LAWRENCE
LIVERMORE
NATIONAL
LABORATORY

UCRL-JRNL-224304

Atomistically-informed Dislocation Dynamics in fcc Crystals

E. Martinez, J. Marian, T. Arsenlis, M. Victoria, J. M. Perlado

September 9, 2006

Journal of the Mechanics and Physics of Solids

Disclaimer

Atomistically-informed Dislocation Dynamics in fcc Crystals

E. Martínez,[1,2] J. Marian,[1] A. Arsenlis,[1] M. Victoria,[2,1] and J. M. Perlado[2]

[1] *Chemistry and Materials Science Directorate,*

Lawrence Livermore National Laboratory, Livermore, CA 94550

[2] *Instituto de Fusión Nuclear, Universidad Politécnica de Madrid, 28006 Madrid, Spain*

(Dated: August 24, 2006)

Abstract

We develop a nodal dislocation dynamics (DD) model to simulate plastic processes in fcc crystals. The model explicitely accounts for all slip systems and Burgers vectors observed in fcc systems, including stacking faults and partial dislocations. We derive simple conservation rules that describe all partial dislocation interactions rigurosuly and allow us to model and quantify cross-slip processes, the structure and strength of dislocation junctions and the formation of fcc-specific structures such as stacking fault tetrahedra. The DD framework is built upon isotropic non-singular linear elasticity, and supports itself on information transmitted from the atomistic scale. In this fashion, connection between the meso and micro scales is attained self-consistently with core parameters fitted to atomistic data. We perform a series of targeted simulations to demonstrate the capabilities of the model, including dislocation reactions and dissociations and dislocation junction strength. Additionally we map the four-dimensional stress space relevant for cross-slip and relate our findings to the plastic behavior of monocrystalline fcc metals.

I. INTRODUCTION

Crystal plasticity in deformed materials is governed by the collective behavior of large ensambles of dislocations. Although continuum laws based on effective dislocation densities can be formulated to describe the macroscopic materials response to a variety of loading conditions, dislocation motion and interactions are complex phenomena that display an intricate dependence on the underlying microstructure. Atomistic methods have been profusely utilized to study isolated interaction mechanisms, but they suffer from space and time scale limitations and therefore fail to properly capture the long-range character of dislocation stress fields and, obviously, the statistical nature of crystal plasticity. Alternatively, Dislocation Dynamics (DD) is a direct approach that attempts to simulate the aggregate behavior of large dislocation ensembles at the mesoscale by decomposing dislocation lines of arbitrary curvature and character into piecewise segments[1–7]. Nevertheless, the number of segments, N, can get quite large ($\sim 10^6$ to 10^8) for meaningful simulations and the computation of long-range forces is a $O(N^2)$ problem that can become computationally intensive for large systems. For an excelent review on these and more aspects of DD see Ref.[8] and references therein.

The application of DD to model one aspect or another of crystal plasticity in fcc metals started in the 70's with the work of Pharr and Nix[9], althought it has not been until recently that detailed studies involving complex geometries and relativelly large dislocation densities have been undertaken[10–18]. Most of these works focus on mapping the strength of dislocation junctions as a function of the reacting geometry, in a clear attempt to capture the elementary mechanisms attendant to forest hardening in stage II of fcc deformation. However, with the notable exception of the work by Shenoy *et al.*[12], and Hardikar, Shenoy and Phillips (in 2D)[19], we are not aware of any work in the literature where the extended nature of perfect dislocations in fcc materials is explicitely taken into account. In addition, the theoretical framework of most dislocation dynamics tools is based on isotropic linear elasticity, which ignores core effects despite the fact that it has recently been shown that they govern important aspects of dislocation processes[20,21], and that the core cut-off radius is not a universal parameter and may affect the calculation of dislocation energies[22,23]. In this work, we set out to provide a dislocation dynamics methodology that accounts for perfect dislocation dissociation and incorporates atomistic information regarding core sizes

and energies. Our methodology hinges on a novel non-singular linear elasticity formulation, whose free parameters are fitted to carefully-designed atomistic simulations.

A. Non-singular continuum theory of dislocations

The linear elastic formulation used in our DD method is the non-singular theory derived by Cai *et al.*[24]. The singularity intrinsic to the classical continuum theory is removed in this formulation by spreading the Burgers vector isotropically about every point on the dislocation line using a spreading function characterized by a single parameter a, the so-called core width. A particular form of the spreading function chosen in this formulation leads to simple analytic formulations for the stress produced by straight dislocation segments, the segment self- and interaction energies, and the forces on the segments. For any value $a > 0$, the total energy and the stress remain finite everywhere and, what is more, the well-known singular expressions are recovered for $a = 0$. Additionally, the formulation is self-consistent in the sense that the expressions for the force obtained by direct differentiation of the non-singular energy and by recurring to the Peach-Köhler formula are identical. The value of the core width a can be selected for numerical convenience to satisfy any given dislocation property. For example, below we match the atomistic and continuum energies of a given dislocation configuration to obtain a general value for our simulations. Now, we can compute core energies and include core effects during dislocation reactions, an issue largely ignored to date in DD simulations. However, although in principle the value of a depends upon the Burgers vector pand the character of a dislocation[23] this general solution has a clear connection to the more fundamental, atomistic models of dislocations, as we shall show below.

B. Brief overview of ParaDis

`ParaDis`, and its companion serial version `DDLab`, are the fruits of a sustained effort at Lawrence Livermore National Laboratory to develop a massively-parallel three-dimensional DD methodology specifically designed for investigating the collective behavior of large numbers of dislocations[25]. The dislocation ensamble is replaced by a network of nodes with the appropriate connectivity, which act as pointwise limits of each of the discretized seg-

ments. Each segment carries a unit of 'vector current' or Burgers vector, which denotes the direction and magnitude of the displacement accumulated as the dislocation moves. Each segment is asigned a line tangent, given by the unit vector connecting the two segment nodes. The nodes move in response to the local stress tensor as dictated by the mobility law, which essentially translates the local force exerted on each node into the corresponding nodal velocities. In addition to moving the nodes, `ParaDis` evolves the network topology to reflect the physics of dislocation motion and collisions in real crystals. Handling the evolving topology of moving and intersecting lines is a daunting bookkeeping task, especially in a parallel implementation. It is therefore highly desirable to keep the logical complexity of the topological switches to a minimum. Presently, `ParaDis` relies on two basic operations: i) insertion of new nodes, and, ii), merging two nodes into one. Even though topological changes consume only a small fraction of the computing time, the associated logic and bookkeeping consitute upwards of 50% of the `ParaDis` source code.

II. TOPOLOGICAL CHANGES RELEVANT TO PARTIAL DISLOCATIONS

A. Implementation of partial dislocations

From a topological point of view, the dissociation of a (perfect) dislocation can be achieved by using a simple node-splitting scheme. Splitting highly connected dislocation nodes is one of the most commonly-used topological changes in discrete dislocation dynamics methods. However, the explicit introduction of partial dislocations in a fcc/DD model presents two main difficulties which are not generally encountered in the modeling of bcc or other systems. First, dislocation dissociation is governed by Frank's rule, which is an energy criterion that relies solely on the crystal's geometry and the stacking fault energy. However, the direct consideration of the system energetics is generally not a structural part of discrete DD models, where forces are calculated directly from the applied stresses through the well-known Peach-Köhler formula. Thus, one must resort to splitting criteria based on power dissipation, which can be calculated without the explicit knowledge of the system energetics. In our model, the energy per unit time dissipated by the forces acting on a specific dislocation node n_i is calculated as $\dot{W}_i = \lambda F_i v_i$, where F_i and v_i are the total force and the velocity acting on n_i and $\lambda > 1$ is an adjustable parameter that reflects the inertial resistance of a dislocation

node to change its current state. In other words, splitting will spontaneously occur only if more energy is dissipated by undergoing the topological change than by remaining in the (biased) present state. If $\lambda = 1$ both states are equiprobable from a transition state point of view, or, in other words, the initial state is not inertially biased. Obviously, λ is an entirely empirical parameter and must be adjusted with care to realistically reflect the energetics of the system at hand and so as not to artificially favor transitions that may not otherwise be preferred thermodynamically. A case in point is the dissociation of a perfect $\frac{1}{2}\langle 110\rangle$ dislocation to a pair of $\frac{1}{6}\langle 112\rangle$ Shockley partials. Since this transformation typically involves energy reductions in the range of 5% ∼30% (taking into account the stacking fault energies, γ_{SF}, of several fcc metals), we have chosen to use λ conservatively and here we have taken $\lambda = 1.01$ for most of our dislocation simulations.

Secondly, the treatment of partial dislocations in fcc metals introduces the need to account for the stacking fault ribbon joining the partials. The stacking fault energy, γ_{SF} (given in energy per unit area), dictates the equilibrium separation distance between adjoining partials by balancing the elastic repulsion with the increase in system energy due to the stacking fault area. In a force method such as DD the attractive force per unit length between partials due to the stacking fault is simply $F_{SFi} = -\frac{\partial E_{SF}}{\partial x_i} = -\frac{\partial(\gamma_{SF} x_i)}{\partial x_i} = -\gamma_{SF}$, (here x_i is the coordinate along the separation direction), which, as as we can see, is constant regardless of the partial separation distance. However, one complication remains and that is to ensure that the force due to the stacking fault always point towards the other partial, *i.e.* the stacking fault force must be self-cointained. In principle, the force due to the stacking fault must act on the plane where the stacking fault is defined ($\{111\}$-type planes in fcc metals). Thus, $\mathbf{F}_{SF}$ must be locally orthogonal to both the line tangent ξ and the plane normal $\mathbf{n}$. Also, as discussed above, $\mathbf{F}_{SF}$ must be directly proportional to γ. Therefore, in order to obtain the correct magnitude of the stacking fault force, we assign a new quantity, $\gamma\mathbf{n}$, to each node such that every segment is now unequivocally defined by its Burgers vector $\mathbf{b}$, its local line tangent ξ and its plane normal $\mathbf{n}$ weighted by the stacking fault energy γ. In this fashion, we define the stacking fault force per unit length as:

$$\mathbf{F}_{SF} = \xi \times \gamma\mathbf{n} \tag{1}$$

As we can see from eq. 1, $\mathbf{F}_{SF}$ does not depend on the character of the dislocation.

Stacking faults are two-dimensional crystal defects that have a specific energy (per unit

area). This means that, analogous to dislocation lines themselves, they cannot have an infinite extension and thus must end at the physical boundaries of the system (free surfaces, grain boundaries, etc.) or at a dislocation. Much like the conservation of the Burgers vector along a dislocation line is a requisite to satisfy the axiom of continuity, the magnitude $\gamma\mathbf{n}$ must be conserved along dislocation lines acting as physical limits of stacking fault surfaces. This is so as to ensure the self-containment of the stacking fault, which in itself plays into the axiom of continuity. The starting condition for perfect dislocation segments is $\gamma\mathbf{n} = 0$, for perfect dislocations are not physical boundaries of stacking fault surfaces. To close the model we need to specify another condition to determine the magnitude of $\mathbf{n}$ (which need not be a unit vector in general) for faulted dislocations. We use Shockley partial dislocations as the reference after which all other $\gamma\mathbf{n}$ are calculated, *e.g.* after a perfect dislocation node splits into two Shockley partial nodes, a unit vector $\mathbf{n} = \left\langle \frac{1}{\sqrt{3}} \frac{1}{\sqrt{3}} \frac{1}{\sqrt{3}} \right\rangle$ is assigned to each one of the resulting nodes. This choice ensures that $F_{SF} = \gamma$ (provided that ξ is also a unit vector) and $\mathbf{F}_{SF}$ is contained on a $\{111\}$-type plane, both of which must hold exactly for a pair of Shockley partials stemming from the same parent perfect dislocation. Therefore, at any given dislocation node two rules must now be satisfied:

$$\begin{aligned} \textstyle\sum_i \mathbf{b}_i &= 0 \\ \textstyle\sum_i \gamma\mathbf{n}_i &= 0 \end{aligned} \tag{2}$$

These rules provide a useful check for topological self-consistency during DD simulations involving multiple partial dislocations.

Although attempts to model the force due to stacking faults have been published recently[12,19,26], we believe that our algorithm provides a level of generality not achieved in previous works.

B. Cross-slip

Cross-slip is one of the most important processes in crystal plasticity, governing hardening, self-organization and patterning, and dynamic recovery in most metals. In fcc materials, the traditional view is that cross-slip is enabled when the stress buildup arising from forest and precipitation hardening is high enough for screw dislocations to escape their obstacles by gliding on a plane different than their original slip plane (the so-called stage III). In the classical theory of cross-slip, dissociated screw dislocations must be constricted until the

edge components of the partials (which prevents slip on a plane other than the primary glide one) mutually annihilate and the resulting perfect screw is free to transfer onto the cross-slip plane. This process, first proposed by Schoeck and Seeger in 1955[27], imposes no restrictions in principle as to whether cross-slip must occur on a close-packed plane. Later, Friedel[28] suggested that a more realistic view would be to assume that the constricted segment splits at once on the cross-slip plane, which is also close-packed. The theoretical aspects of Friedel's model were worked out by Escaig in what has come to be known as the Friedel-Escaig mechanism for cross-slip[29]. However, this constricted state in the Friedel-Escaig model is a high-energy one and the dislocation may cross-slip before reaching it by way of the constriction-free mechanism proposed by Fleischer[30], in which a dislocation spreads into the cross-slip plane before the dislocation is fully constricted in the primary plane. Because, this spreading is carried out by a Shockley partial, cross-slip, as in Friedel's model, may only occur on close-packed planes. More recently, Cawkwell *et al.*[31] have proposed an alternative mechanism based on the metastable existence of a non-planar core structure in Ir that leads to very high cross-slip rates without need for constriction. For a comprehensive study of the theoretical and experimental aspects of cross-slip, the reader is referred, respectively, to the the excellent reviews by Püschl[32] and Caillard and Martin[33] (and references therein).

Of course, in real crystals, all cross-slip mechanisms described above can coexist simultaneously and the relative likelihood of each one is only determined by the local deformation conditions, such as temperature, strain rate, applied stress and stacking fault energy, among others. For consistency with the current experimental and theoretical understanding regarding cross-slip processes, we have developed an algorithm compatible with the implementation of partial dislocations explained in Section II A that includes both the Friedel-Escaig and the Fleischer mechanisms of close-packed cross-slip.

Therefore, our model allows dislocations to cross-slip by either mechanism, depending only upon the local nodal conditions, *i.e.* with no *a priori* assumption of what the cross-slip pathway should be. Both the Friedel-Escaig and the Fleischer mechanisms have been implemented as follows:

- Friedel-Escaig: At any given time, a node belonging to a perfect dislocation whose line tangent is locally parallel to the $\langle 110 \rangle$ direction of the Burgers vector is split on both the glide and the cross-slip planes.

- Fleischer: At any given time, a node belonging to a Shockley partial dislocation whose line tangent is locally parallel to the $\langle 110 \rangle$ direction of the Burgers vector of the original perfect dislocation is split on both the glide and the cross-slip planes.

These nodal splittings are consistent with eq. 2 so that the new nodes have the correct $\gamma\mathbf{n}$ and $\mathbf{b}$ vectors while retaining the same local line tangent as that of the initial node. In both cases, if the energy dissipated per unit time by the new nodal configuration is greater than that dissipated by the original one (which depends on the stress tensor applied on the dislocations), then the new configuration is accepted and cross-slip is performed. Else, the new configuration is rejected and the original dislocation node continues to glide on the primary glide plane.

It is worth stressing that the advantage of this procedure is that both of these mechanisms, together with the partial dislocation splitting explained in Section II A operate simultaneously on every node at every time step and no assumptions are made as to which one should be favored. It is the applied stress, the configuration's geometry and the elastic parameters that determine, by way of the power dissipation criterion, which process should occur.

C. Topology changes in multinodes

The above splitting procedure works very efficiently for nodes with single connectivity, *i.e.* for non-branching dislocation segments, but it is not sufficient to describe all possible dislocation configurations with more coplex geometries. For nodes with multiple connectivity, the so-called *physical nodes* or junctions, a modified splitting algorithm must be used in order to allow for the topological changes associated with nodes where several dislocation segments converge. On top of the multinode splitting scheme existing in `ParaDis`, which, in general, does not preserve the original node connectivity, we have developed a new algorithm to explore additional partial dislocation core transitions. Particularly, we are interested in a procedure that permits cross-slip of physical nodes. This splitting algorithm must now ensure that the connectivity is maintained and that the junction, as a physical entity, is not altered by any topological transformations. The optimum way to do this is to insert two nodes in two of the converging segments. How and where are these nodes inserted will depend on the specifics of the system under study. In our case, we must particularize this algorithm for fcc systems introducing appropriate geometric constraints consistent with

dislocation theory. Specifically, if, and only if, two of the segments arriving at a multinode are non-degenarate $\frac{1}{2}\langle 110\rangle$ directions of the same $\{111\}$ plane then a node is inserted on each one of these segments at a distance d_a (as for simple node splitting) from the original multinode. The connectivity of the newly-inserted nodes is then increased by linking them to one another, thereby effectively 'bypassing' the original multinode. Next, $\mathbf{b}$'s and $\gamma\mathbf{n}$'s are assigned to the new nodes taking into account their local environment so as to conform with the continuity rules 2. Finally, all possible configurations are compared against each other and the final choice (which may very well include the starting configuration) is made on the basis of our power dissipation criterion.

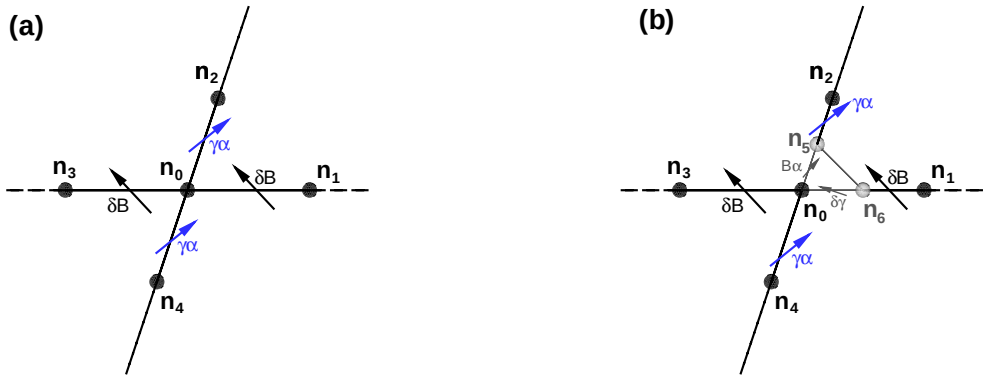

FIG. 1: (a) Schematic representation of a physical node (tetranode) resulting from the intersection of a δB Shockley partial and a $\gamma\alpha$ stair-rod dislocation. (b) Splitting mechanism of the multinode, where two new nodes, n_5 and n_6, have been inserted and connected, and the connectivities and Burgers vectors of segments $\overline{n_0 n_1}$ and $\overline{n_0 n_2}$ have been updated to reflect the new topological state of the multinode. The Burgers vector directions and line tangents shown in the figures are not intended to define the character of the dislocations, and are simply for labeling purposes.

The procedure is schematically outlined in Figure 1, where we have chosen a tetranode as example. Note that this mechanism acts in addition to –not instead of– the topological changes described in Sections II A and II B.

III. RESULTS AND DISCUSSION

As discussed above, our methodology includes a panoply of topological transformations for each dislocation node that reflects the special character of the fcc lattice. At any given instant, depending on the local geometry and stress conditions, topology changes are accepted or rejected on the basis of the maximum power dissipation criterion explained in Section II A. This criterion determines which transformations will occur but it does not provide precise quantitative information, such as partial dislocation separation distance, critical stresses for cross-slip or strength of junctions. Below we present two sets of calculations. First we fit the adjustable parameters of our DD methodology to results of Shockley partial equilibrium spacings obtained with Molecular Dynamics (MD), which is considered here as our first-principles method. Secondly, we perform quantitative predictions relevant to fcc metals with the fully parametrized method. Specifically, we will focus on the calculation of the strength of dislocation junctions, the formation of stacking-fault tetrahedra (SFT) and the mapping of the cross-slip space for a single screw dislocation. We have chosen Cu as our model fcc system, due to the extensive literature available regarding its plastic properties.

A. Shockley partial equilibrium separation distance

In order to parametrize our DD methodology, we have performed MD simulations of perfect screw dislocation dissociation to measure the Shockley partial equilibrium separation. Subsequently, we have benchmarked our calibrated code against atomistic equilibrium spacing results at zero stress as a function of dislocation character.

1. Fitting of the dislocation dynamics free parameters

For the MD calculations we use a Parrinello-Rahman, conjugate-gradient algorithm with convergent image summations[34]. A perfect $\frac{1}{2}[1\bar{1}0]$ screw dislocation was introduced in the MD computational box and allowed to relax for a given level of Escaig stress. The Escaig stress tensor is defined as that which produces a force only upon the edge components of the Shockley partials. Once the equlibrium configuration is attained, we calculate the separation distance by measuring the spacing between the dislocation cores of the resulting pair of partials. The cores have been identified by plotting the atomic disregistry along

the edge and screw directions, namely $[1\bar{1}0]$ and $[11\bar{2}]$, on the dislocation glide plane at each stress. Figure 2 shows the screw and edge components of the atomic disregistry at zero and 2000 MPa, where constriction is seen to occur. At zero stress, we measure a Shockley partial dislocation spacing of 1.56 nm, not far from the 1.77 nm calculated by Henager and Hoagland using core fields[35]. As the applied Escaig stress is increased the partial dislocation spacing decreases in discrete steps consistent with the $[11\bar{2}]$ interplanar distance down to full constriction. Figure 2b shows the atomic disregistry for the dislocation configuration at 2000 MPa. The discontinuity in the screw component profile can be clearly appreciated, indicating the disappearence of most of the stacking fault ribbon. The edge component curve displays an offset close to the center of the box, which is a sign that the dislocation is not fully constricted and some splitting is retained, albeit too small to produce an identifiable stacking fault. The slope in the curve for the edge component simply represents the background homogeneous shear deformation imparted on the computational box resulting from the applied Escaig stress. For the sake of consistency, throughout this work we use values for a_0, γ_{SF} and μ derived from the interatomic potential used in the MD calculations[36]. The values for the lattice parameter, the intrinsic stacking fault energy and the shear modulus are, respectively, $a_0 = 3.616$ Å, $\gamma_{SF} = 2.77 \times 10^{-3}$ eV·Å^{-2} and, after rotating the canonical shear modulus of 76.2 GPa to the particular geometry used in the MD simulations, $\mu = 63.2$ GPa.

Following this procedure to measure separation distances, we have explored the constriction stress range up to 2500 MPa, from zero down to the point when the dislocation is seen to spontaneously dissociate on a different {111} plane, signaling a Friedel-Escaig transition. The results are shown in Figure 3. As we can see, between 2000 and 2500 MPa, the equilibrium separation distance lies on the same plateau corresponding to one interplanar distance ($\sim$0.54 nm). In other words, we take constriction to occur at $\sigma_E = 2000$ MPa based both on the core disregistry criterion explained in the above paragraph as well as on the fact that the minimum separation distance attained before spontaneous dissociation on a different {111} plane is first reached at that stress. We have also done calculations applying a negative (stretching) Escaig stress that tends to separate the partial dislocations. Lacking the energetics that would limit the size of the stacking fault ribbon in between the two Shockley partial dislocations, once the separation forces created by the applied stress surpass the value prescribed by γ_{SF} we have unbound runaway partials. We have observed

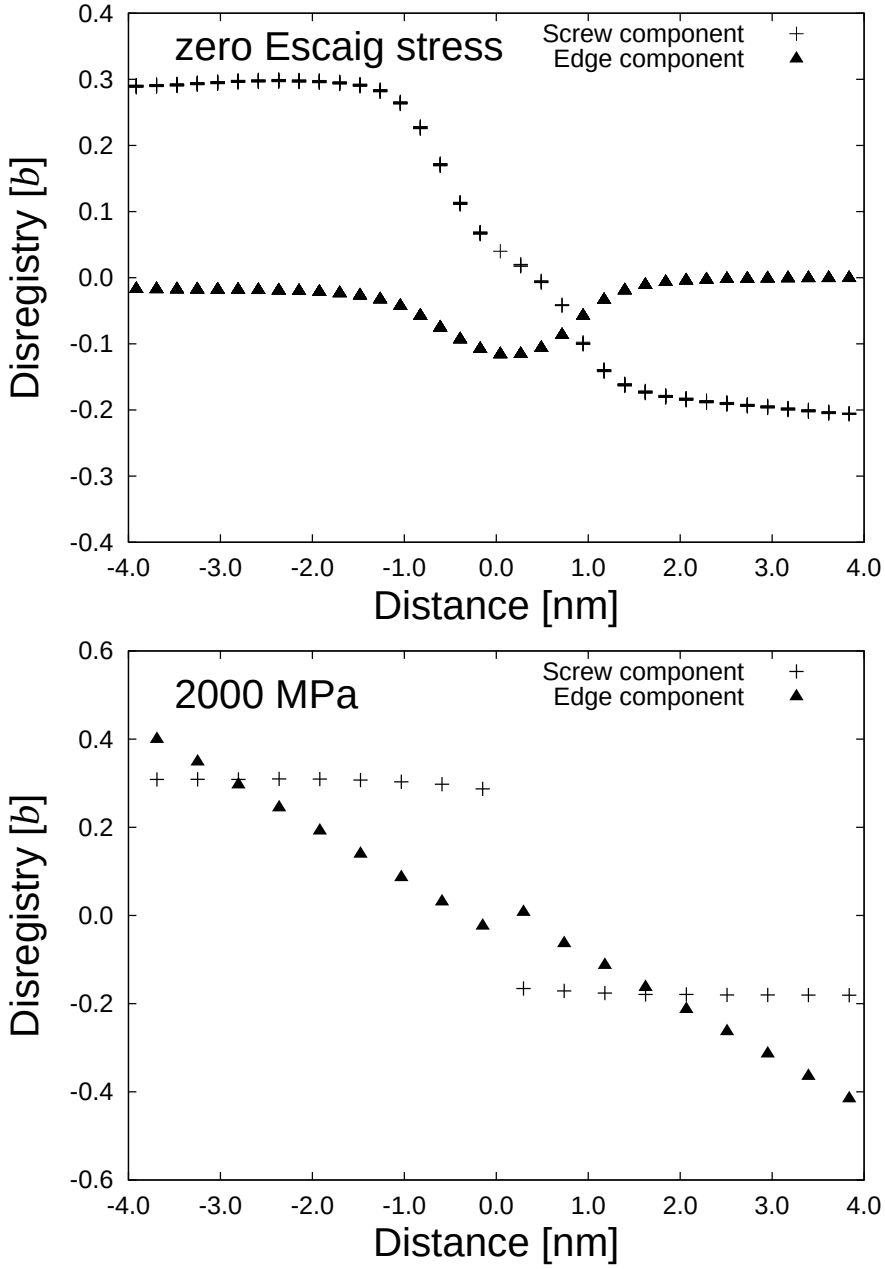

FIG. 2: Atomic disregistry in Burgers vector units on the dislocation glide plane for a perfect $\frac{1}{2}[1\bar{1}0]$ screw dissociated into partials: (a) at zero stress we measure a distance of 1.56 nm, whereas at 2000 MPa (b) full constriction has been attained.

this to occur at approximately -500 MPa.

Now that the stress range over which the dislocation is split into partials has been defined ($-500 < \sigma_E < 2500$ MPa), the next step is to make use of this information to parametrize our DD simulation tools. To this end, we have fitted the value of the core width a in the

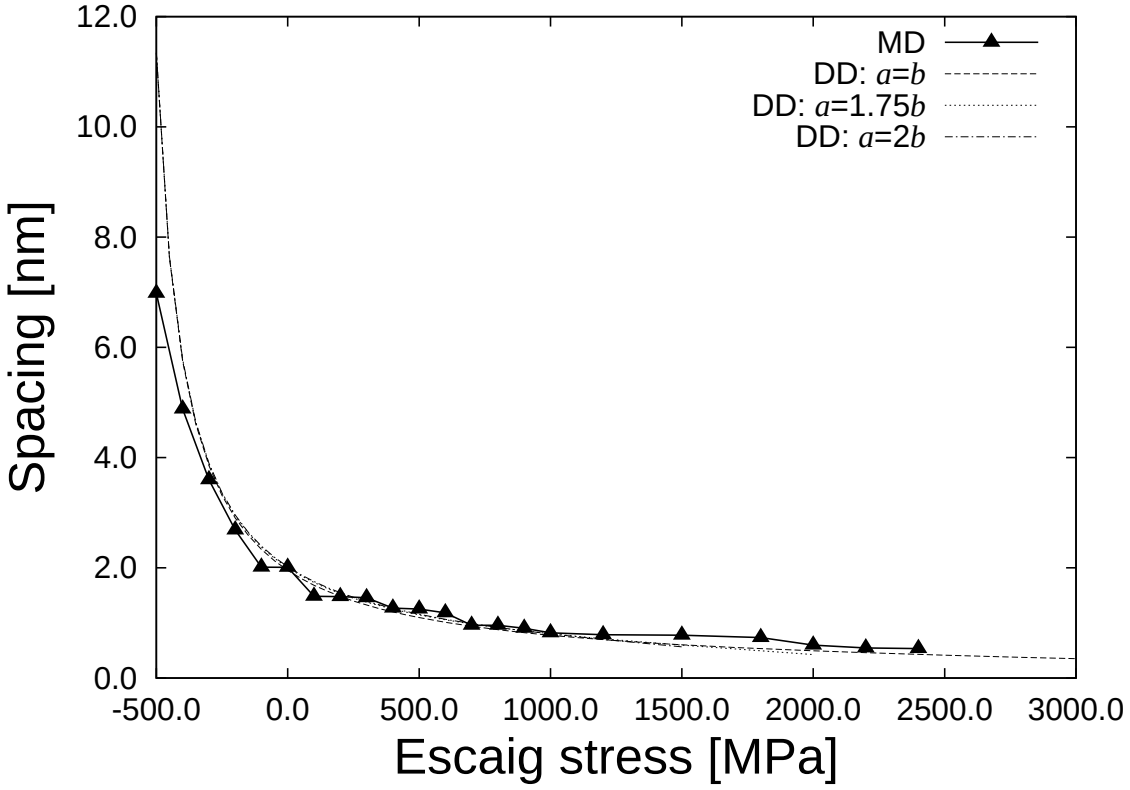

FIG. 3: Shockley partial separation distance as a function of Escaig stress for a screw dislocation. The MD curve has a descending staircase shape, a reflection of the *quantized* nature of the separation distance stemming from lattice discreteness. The best DD fit (obtained for $a = 1.75b$) is achieved by matching the MD results for the separation distance at zero stress and the stress at which constriction is attained.

non-singular linear elastic formulation used in our codes by fitting the linear elastic response of DD to the MD data.

Since the MD curve shown in Figure 3 is defined by the equilibrium separation distance of 1.56 nm at zero stress and the stress of 2000 MPa at which constriction occurs, we have found the value of a that strikes the optimum compromise between these two pieces of information. Figure 3 shows three linear elastic curves for three different trial values of a. Clearly, the curve corresponding to $a = 1.75b$ (where b is the modulus of the Burgers vector of the perfect dislocation) is found to provide the best fit to the MD data and hereon we set $a = 1.75b = 0.447$ nm for all subsequent calculations. Though the agreement between both approaches is remarkable, the comparison between the two curves is burdened by limitations coming from both sides. For example, the assumption of isotropy in DD ignores the crystal

orientation of the relevant slip systems in fcc metals. For its part, despite using methods for minimizing image interactions, the use of periodic boundaries in MD causes artifacts that may affect the equilibrium configurations of the simulated structures.

Next, we turn to the calculation of the friction coefficients attendant to the mobility functions. In the present DD implementation, the mobility function, $\mathbf{M}$, is a second order tensor that maps the nodal forces derived from the applied stress onto the corresponding nodal velocities:

$$\mathbf{f} = \mathbf{M}\mathbf{v} \tag{3}$$

$$\mathbf{M} = B\,(\mathbf{n} \otimes \xi) \tag{4}$$

Here, only the glide contribution of $\mathbf{M}$ is considered. The parameter B is a friction coefficient that is constant in the low-velocity regime that is of interest in the present calculations. In general, B depends on the character of the dislocation as:

$$B = B_s \cos^2\theta + B_e \sin^2\theta \tag{5}$$

where θ is the angle between the dislocation line and the Burgers vector and B_s and B_e are the friction coefficients for the perfect screw and edge dislocations respectively. Following the procedure outlined in Ref.[37] we have carried out large scale three dimensional MD simulations to calculate the values of the respective friction coefficients. For this potential, we have obtained $B_s = 9.82 \times 10^{-6}$ and $B_e = 2.31 \times 10^{-6}$ Pa·s respectively.

The final ingredient extracted from MD calculations to be used in our DD simulations is the dislocation core (non-linear) energy for a fixed core width of $a = 1.75b$ for all possible partial dislocations included in our model. We use the procedure outlined in Ref.[38] coupled with the non-singular elastic formulation described in Section I A to calculate the elastic energy of a dislocation dipole. Table I shows all the relevant core energies for both $a = 1.75b$ and, for academic interest, $a = b_p$, where b_p is the Burgers vector of the corresponding partial dislocation. The high core energies associated with the Hirth and Frank partials are a reflection of their relatively high Burgers vector moduli and edge character. By comparison, the perfect screw dislocation displays a rather low core energy, which substantiates the fact that perfect dislocation dissociation is a process purely governed by Frank's rule of elastic energy reduction, with little or no core contributions.

TABLE I: Partial dislocation core energies for core widths, a of $1.75b$ and b_p as calculated with MD simulations for Cu. Burgers vector moduli are given in Å, while core energies are given in units of eV$\cdot b^{-1}$. The core configurations were obtained folowing the procedure of Li *et al.* with the modification for the perfect dislocation outlined in[39].

Dislocation type	$\mathbf{b_p}$	b_p	$E_{\text{core}}(1.75b)$	$E_{\text{core}}(b_p)$
Shockley partial	$\frac{1}{6}\langle 112\rangle$	1.476	0.317	0.189
Stair-rod	$\frac{1}{6}\langle 110\rangle$	0.852	0.193	0.062
Hirth partial	$\frac{1}{3}\langle 001\rangle$	1.205	1.451	1.085
Frank partial	$\frac{1}{3}\langle 111\rangle$	2.088	1.835	1.450
Perfect dislocation	$\frac{1}{2}\langle 110\rangle$	2.557	0.530	0.236

2. Calculation of the separation distance as a function of dislocation character

Using our fully-parametrized methodology we now turn to the calculation of the Shockley partial separation as a function of dislocation character and Escaig stress. Our intention is to benchmark our tool against existing atomistic data at zero stress, and to calculate the critical constriction stress in each case. For the latter calculation, the critical stress is taken to be that at which constriction is attained, *i.e.* when the non-singular stress barrier is surpassed. Results are shown in Figure 4, where we have considered perfect screw and edge dislocations as well as 30^o and 60^o mixed dislocations. We can see that the agreement of our curves with the available atomistic data (from Henager and Hoagland[35]) at zero Escaig stress is quite reasonable. The critical constriction stresses for the perfect screw, 30^o, 60^o and perfect edge dislocations are, respectively, 2000, 1900, 1700 and 1500 MPa. Approximately, the critical constriction stress varies linearly with the dislocation character.

B. Strength of dislocation locks

In the absence of significant lattice resistance, the main impediment to dislocation glide in pure fcc materials are forest interactions, *i.e.* intersections of mobile dislocations with dislocations lying on other slip systems. There are a large number of potentially important intersections mechanisms but here we focus on the reactions between attractive extended dislocations that form strong barriers to the motion of other dislocations. The strength

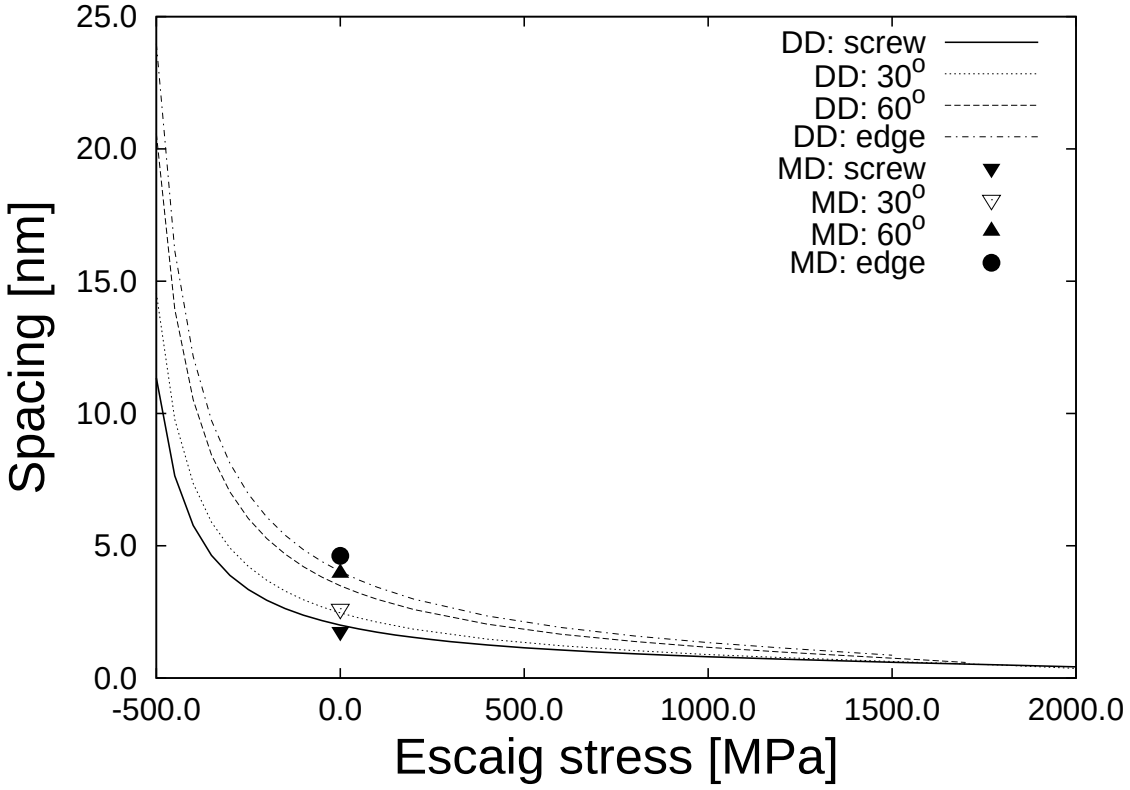

FIG. 4: Equilibrium separation distance between Shockley partials as a function of constricting Escaig stress for a pure screw (alredy shown in Figure 3), 30^o and 60^o mixed dislocations, and a perfect edge dislocation. All curves have been obtained with the model as parametrized in Section III A. Our curves are compared with the data points obtained by Henager and Hoagland[35] using atomistic simulations.

of these barriers is important to estimate the strength coefficient matrix, α_{ij} in Taylor's equation for hardening:

$$\tau_{ij} = \mu b \alpha_{ij} \sqrt{\rho_j} \tag{6}$$

where τ_{ij} is the critical resolved shear stress (C.R.S.S.) in slip system i, μ and b, as above, are the shear modulus and the Burgers vector's magnitude and ρ_j is the dislocation density in slip system j. Essentially, eq. 6 relates the stress in slip system i due to dislocations in all other slip systems. To obtain the total C.R.S.S. in slip system i, one simply does $\tau_i = \sum_j \tau_{ij}$. When particularizing this to the 16 slip systems in fcc metals, many of the α_{ij} coefficients will be zero. However, by virtue of symmetry, all the non-zero coeffiecients reduce to four types of interactions[40,41], namely the Lomer-Cottrell locks, the glissile junctions, co-linear junctions and Hirth locks.

There have been several works on dislocation junctions in fcc metals both using dislocation dynamics and atomistic simulations. For example, Zhou *et al.* investigated the formation of perpendicular extended dislocations using large-scale MD simulations[42] and found it to be a complex process involving zipping, bowing and unzipping, leading to the formation of a unit jog. On the other hand, Shenoy, Kukta and Phillips[12] and Rodney and Phillips[43] have studied the strength of the Lomer-Cottrell junction in Al using coarsening methods (dislocation dynamics and the Quasicontinuum method respectively) and found relatively good agreement with atomistic and continuum calculations. These and other works[10,13–17] have mostly focused on the Lomer-Cottrell lock, as this has traditionally been thought of as the strongest of all attractive junctions. Recently, Madec *et al.*[44] have proposed that the junction governing the hardening in fcc crystals is that resulting from dislocations with co-linear Burgers vector gliding on intersecting planes, rather than the Lomer-Cottrell. Their argument is sustained on the fact that, based on the computed magnitude of the hardening coefficient α, co-linear interactions contribute the most to the total hardening in eq. 6. Devincre *et al.* have further refined and confirmed Madec's calculations in a recent publication[18].

Here we study each attractive reaction and we investigate the minimum stress required to break them once they are formed spontaneously. In principle, all the details of each dislocation reaction are contained in the corresponding yield curve as a function of the interaction angle (for example Refs.[12,13,17]). Strength yield curves are typically obtained as the loci of the pairs of primary, τ_1, and forest, τ_2, stresses that produce junction dissolution. We are intent on exploring these fcc junctions with our newly developed methodology in an attempt to establish whether core energetics —via the line stifness model— and partial dislocation reactions provide any additional insights beyond the classical, purely elastic treatment utilized to date in the literature. To this end, we have only computed the three points that define the positive quadrant of the yield curve —*i.e.* (τ_1,τ_2=0), (τ_1=0,τ_2) and (τ_1=τ_2)—, our main aim simply being to demonstrate the numerical capabilities of our method. All reactions have been simulated for parallel dislocation segments (no reaction angular dependence), which should provide an upper bound for the lock strength. Otherwise, all the simulations have been carried out for 60.2-nm long segments. The respective geometries are specified for each reaction below with the equilibrium configurations shown schematically in Figure 5.

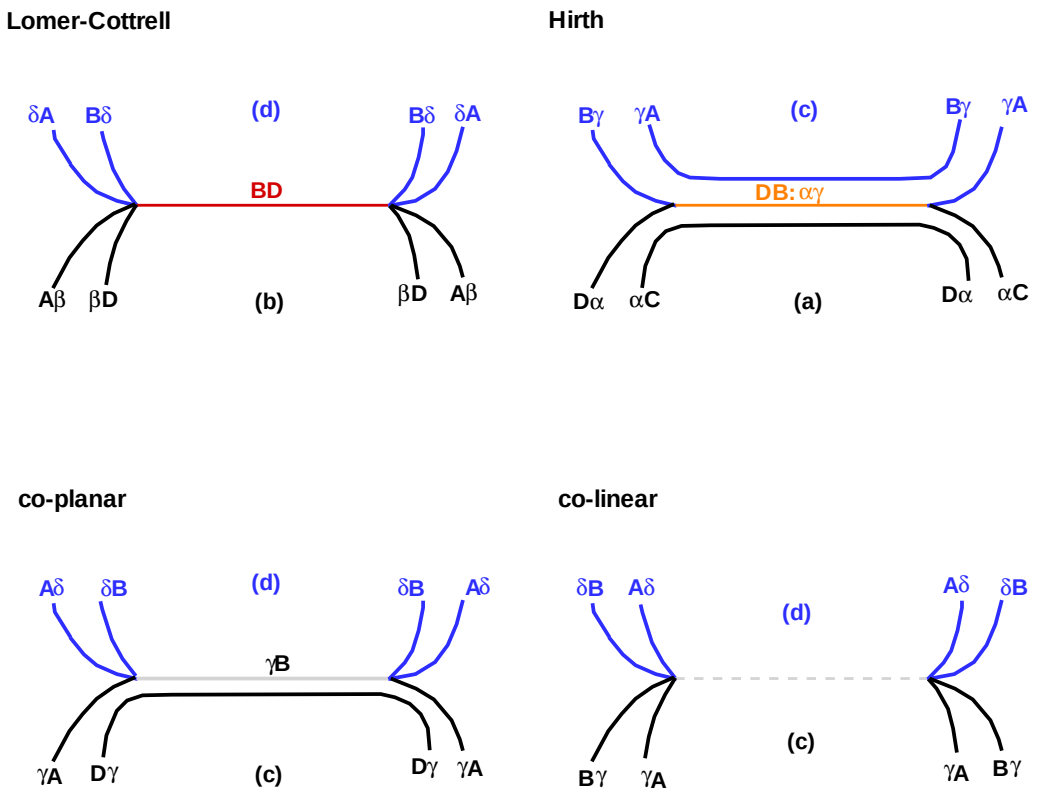

FIG. 5: Schematic representation of each junction geometry in equilibrium as obtained with our methodology. With the notable exception of the co-planar lock, all junctions are symmetric with respect to the intersection line of the glide and forest planes (for the parallel initial configuration treated here). Thompson's notation is used for clarity.

1. *Lomer-Cottrell junction*

The Lomer-Cottrell lock appears when two perfect dislocations of the same {111} zone occur gliding on different planes. The two leading partials are attracted to one another and react along the $\langle 110 \rangle$ line of intersection between the two planes to form a pure-edge $\frac{1}{6}\langle 110 \rangle$ stair-rod partial dislocation. The stair rod's Burgers vector does not belong to any of the initial glide planes and is therefore a sessile dislocation. Both the elastic self-energy and the core energy of a stair-rod dislocation are relatively low (see Table I) which makes this reaction very stable and the lock quite strong. We have studied Lomer-Cottrell junctions

with geometries involving a pair of perfect dislocations with $\mathbf{b}_1 = \frac{1}{2}[\bar{1}10]$ and $\mathbf{b}_2 = \frac{1}{2}[101]$, gliding respectively on (111) and $(1\bar{1}\bar{1})$ planes. In Thompson's notation this corresponds to a AB(d)+DA(b) reaction.

If one disregards the stacking fault energy in the elastic model, the trailing partials are repelled by the stair-rod dislocation and lie on their original glide planes at some equilibrium distance. However, for the relatively long line segments considered (60.2 nm), the two trailing partials collapse onto the stair-rod dislocation to form a perfect $\frac{1}{2}\langle 110\rangle$ Lomer dislocation, capable of gliding on {001}-type planes (see Figure 5). According to Frank's rule:
$\mu {b_L}^2 < \mu {b_{sr}}^2 + 2\mu {b_{sp}}^2 + \gamma$,
this will only be energetically favorable if the stacking fault-energy γ is greater than a critical value that depends on the magnitude of the Burgers vectors of the perfect Lomer dislocation, b_L, the stair-rod, b_{sr}, and the Shockley partials, b_{sp} (without considering core effects). Neglecting the stacking fault energy, the split configuration (two Shockleys plus the stair-rod) is energetically favorable by approximately 20%, and thus the collapse into a Lomer dislocation does not occur. This is precisely what we have seen when we fix $\gamma = 0$ in our DD simulations. In any case, we expect this mechanism to be quite sensitive to several reaction parameters such as reaction length and angle, distance of the original dislocations from the intersection line, etc.

Another important aspect to consider is the two types of configurations that are geometrically possible, namely the case where the angle between the two intersecting planes is acute and the case when it is obtuse. The formation of an obtuse Lomer-Cottrell junction entails having extrinsic stacking faults[45–47], which are considerably higher in energy than intrinsic ones, such as those found for an acute lock (84.5 vs. 44.4 mJ·m^{-2}, according to our interatomic potential). The main implication of this is that obtuse configurations can be considered practically forbidden for our purposes, a fact supported by our own atomistic simulations of junction formation and cross-slip. The outcome is precisely that, although geometrically plausible, the energy cost incurred when creating an extrinsic fault in our Cu model is far too high for these transitions to be allowed. This observation is supported by Bonneville and Vanderschaeve's[47] linear elastic analysis of Lomer-Cottrell junctions reconciled with experimental observations.

Lastly, as the geometry in Figure 5 suggests, in principle the yield curve of the Lomer-Cottrell is symmetric with respect to stresses applied on the the forest and glide planes and

thus $\sigma_1|_{\sigma_2=0} = \sigma_2|_{\sigma_1=0}$. The values obtained are ∼448 MPa for the first two symmetric points and 375 MPa for the case of equally stressed planes, or 0.0071μ and 0.0059μ, respectively. The normalized strength for the $(\sigma_1, 0)$ stress point along with the slip geometry and the corresponding **b** and $\gamma\mathbf{n}$ reactions are shown in Table II.

2. Hirth lock

The Hirth lock is formed when two perfect dislocations with perpendicular Burgers vectors glide on intersecting planes. This reaction results in a sessile $\frac{1}{3}\langle 001\rangle$ Hirth partial dislocation flanked by the two trailing partials. The Hirth lock is the conjugate of the Lomer-Cottrell in that only the obtuse configurations will produce an intrinsic fault. Thus, in this case we need not consider the acute configuration. For these simulations we have also chosen two perfect dislocations with slip systems $\frac{1}{2}[\bar{1}10](\bar{1}\bar{1}1)$ and $\frac{1}{2}[\bar{1}\bar{1}0](\bar{1}1\bar{1})$ (CD(a)+BA(c) in Thompson's notation). The normalized junction strengths are given in Table II for the three points in the positive quadrant of the yield curve. In the same fashion as the Lomer-Cottrell, the Hirth lock is symmetric about the bisectrix plane that contains the intersection line of the forest and the glide planes (see Figure 5). Thus, the strength of the junction is invariant with respect to which is the activated plane and equal to ∼265 MPa or 0.0042μ. On the other hand, the strength for $(\sigma_1 = \sigma_2)$ is ∼233 MPa or 0.0037μ. The normalized strength for the $(\sigma_1, 0)$ stress point along with the slip geometry and the corresponding **b** and $\gamma\mathbf{n}$ reactions are shown in Table II.

Based on purely elastic considerations, Hirth[41] considered this reaction to be the strongest barrier to dislocation glide in fcc metals. Contrarily, our calculations show that the strength of this junction is lowest among all four considered, for the parallel geometry and zipping length of 60.2 nm. From the point of view of the reacting geometry, Kubin *et al.* have recently extended Hirth's analysis by mapping the dislocation reaction space as a function of dislocation character and found a strong dependence of the barrier strength with the angular character of the reacting dislocations[10]. However, their work shows that only a very small deviation from perfectly-parallel segments is allowed for the formation of a Hirth lock. Nevertheless, they also found the Hirth lock to be the weakest among all fcc junctions.

3. Co-planar junction

A co-planar junction —also referred to as 'glissile' junction—, is formed when two perfect dislocations lying on different planes react along the plane intersection to produce the third perfect dislocation of the $\{111\}$ zone whose glide plane normal is $\mathbf{b}_1 \times \mathbf{b}_2$. The simulated geometry is similar to the Lomer-Cottrell, except that in this case one of the reacting dislocations, the $\frac{1}{2}[1\bar{1}0]$, is a perfect screw dislocation on the (111) plane, while the remaining dislocation is a $\frac{1}{2}[\bar{1}0\bar{1}]$ lying on a $(\bar{1}\bar{1}1)$ plane. The new dislocation is also perfectly glissile on the $(\bar{1}\bar{1}1)$ plane, which acts as the forest plane in our simulated geometry. This means that the only stress component governing junction dissolution in this case is σ_1, as σ_2 simply acts as a glide component on the forest plane. Thus, only those stress combinations for which the applied σ_1 can overcome the glide force created by σ_2 are relevant for junction strength calculations. Presumably, this will result in a discontinuous yield curve with a gap at low σ_1 stresses. Indeed, we found that there is no $(0, \sigma_2)$ nor $(\sigma_1 = \sigma_2)$ solution for this lock, as the new dislocation simply glides on the forest plane and the junction nodes act as a Frank-Read source. For the $(\sigma_1, 0)$ we obtain a value of 656 MPa (0.0104μ). This value, along with the slip geometry and the corresponding $\mathbf{b}$ and $\gamma\mathbf{n}$ reactions are given in Table II.

Because of its glissile nature on the forest plane, the co-planar junction is the only non-symmetric one among the four fcc locks studied. The schematic equilibrium configuration is shown in Figure 5, where the (d) plane is the initial glide plane and (c) is the forest plane.

4. Co-linear junction

The co-linear junction results from the mutual annihilation of locally-screw segments of perfect dislocations with opposite Burgers gliding on different $\{111\}$ planes. These dislocations attract one another and, when sufficiently close, may alter the local character of the dislocation line affecting the reaction length. The geometry we have used in this case involves a BA(d) and a AB(c) dislocations annihilating along their mutual plane intersection (see Table II for the numeric expressions). By way of this reaction, segments of both dislocations become connected on either sides of the annihilated length. If one takes into account the extended nature of dislocations in the fcc lattice, the reacting dislocations form

tetranodes that are sessile on either of the two original planes (although they can glide along the line). Therefore, these nodes effectively act as pinning points, contributing to hardening. The dissolution of this lock involves the unzipping of the virtual junction by glide of the tetranodes along the intersection line. This is precisely the dissolution mechanism for the point of the yield curve with equally activated planes, for which $\sigma_1 = \sigma_2 = 635$ MPa or 0.0103μ (see Table II for more details). The behavior is somewhat different when only one of the planes is activated. In those cases, the tetranodes act partially as dislocation sources via their activated dislocation segments, which increases the amount of stress required to break the lock: $\sim$950 MPa or 0.015μ.

C. Formation of stacking-fault tetahedra

We now turn to another important aspect of fcc metals, namely the treatment of Frank partial dislocations and the formation of stacking fault tetrahedra (SFT). The Frank partial is an edge dislocation and since its Burgers vector is not contained in a close-packed {111} plane it cannot glide conservatively under the action of an applied tress. A closed dislocation loop of a Frank loop partial dislocation can be produced by the collapse of a platelet of vacancies. This is commonly observed in quenched or irradiated metals where a local supersaturation of vacancies is produced[48]. The Burgers vector of a Frank partial is not a lattice vector and therefore a Frank loop encloses a stacking fault. If the stacking fault energy is sufficiently high, the Frank loop will be stable, but in low stacking-fault energy metals the loop must unfault to become stable. Basically, there are two ways to unfault a Frank loop, depending on its size. If the loop is large, *e.g.* typically forming hexagonally-shaped loops, it can be swept by a Shockley partial on the habit plane to form a perfect dislocation loop. On the other hand, for intermediate-to-small sizes, the Frank partial may dissociate into a low-energy stair-rod dislocation and a Shockley partial on an intersecting slip plane. Similar to the Lomer-Cottrel junction, this dissociation can only take place in the acute direction of the intersecting {111} plane, that is, in the *c*onvergent sense. As we shall show, this condition ensures the proper formation of SFTs. Again, which mechanism should operate is solely determined on the basis of the power dissipation criterion.

Due to its higher complexity and interest, here we focus on the formation of a stacking-fault tetrahedron from a Frank loop in Cu. We start from a triangular 5.8-nm loop with

sides aligned with ⟨110⟩ directions. We then let the system relax at zero stress by applying the criterion explained in the previous paragraph and the rules in eq. 2. A sequence of the simulation is shown in Figure 6. Each side of the original triangle is a Frank segment with

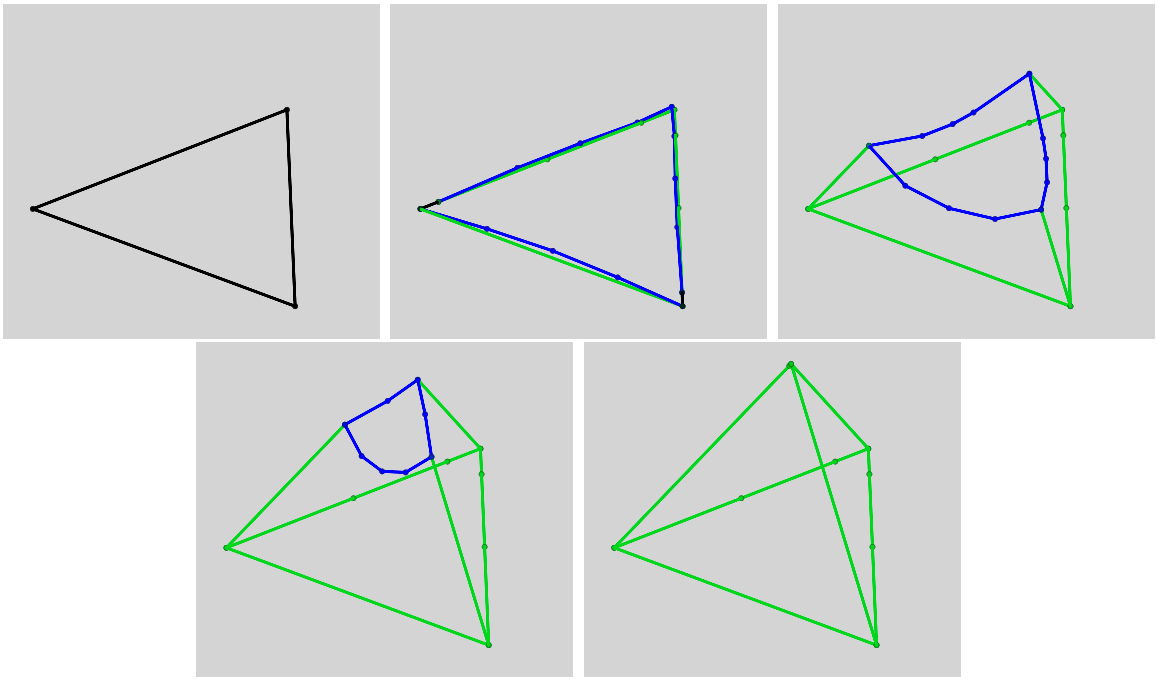

FIG. 6: Simulation of the transformation of a 4-nm triangular Frank loop into a perfect stacking-fault tetrahedron. Dislocation segments are color-coded according to their Burgers vector: black is Frank partials, blue are Shockley partials and green segments are stair-rod dislocations.

Burgers vector $\frac{1}{3}[111]$ (shown in black). Each segment undergoes a dissociation of the type:

$$\frac{1}{3}[111] \rightarrow \frac{1}{6}[110] + \frac{1}{6}[112] \tag{7}$$

into a Shockley partial and a stair-rod dislocation. Basically, the Shockley partials are each glissile on the remaining {111} planes of the Thompson tetrahedron and react with one another on the edges of it. Although dissociation initilally occurs close to the center of the triangle sides, as we can see, the Shockley partials are more inclined to react among themselves than to glide along the facets of the tetrahedron, reason why reactions at the edges occur in advance of glide on the {111} planes. This means that the edges grow faster than the facets, something commonly assumed to occur inversely.[57] To ensure that this is not an artifact of the simulation introduced by the line tension effects we look at the node insertion criterion. The initial triangle contains only three nodes, then, as the dissociation

proceeds, more nodes are introduced automatically to maintain the equilibrium shape of the new partials. Our criterion for the insertion of nodes can be fine-tuned to achive a satisfactory line shape but we have seen little influence of this on the final dynamics. In other words, this effect appears to be a consequence of the system dynamics, governed by the stacking fault energy and the power dissipation criterion, and not an artifact resulting from discrete effects.

The initial dissociation of the Frank loop as written in eq. 7 is governed by eqs. 2, whereby new Burgers and $\gamma\mathbf{n}$ vectors are assigned to the product dislocations in eq. 7. However, no assumption is made as to what direction should the dissociation occur, *i.e.* in the convergent sense (tetrahedron) or in the divergent sense (where the resulting structure would be some kinf of truncated geometry. The fact that the dislocations choose the former path is solely a consequence of the dynamics implemented in the code and no 'artificial' enticement of any kind is performed.

D. Cross-slip

Figure 7 shows the geometry of the cross-slip space of interest. In essence, we are only interested in the four components of the stress tensor that are relevant for cross-slip, namely Escaig (E) and glide (G) stress applied independently on the primary (glide) and secondary (cross-slip) planes:

$$\begin{aligned} \sigma_{E1} &= \tilde{\sigma} : \mathbf{S}_{E1} \\ \sigma_{G1} &= \tilde{\sigma} : \mathbf{S}_{G1} \\ \sigma_{E2} &= \tilde{\sigma} : \mathbf{S}_{E2} \\ \sigma_{G2} &= \tilde{\sigma} : \mathbf{S}_{G2} \end{aligned} \tag{8}$$

where the $\sigma_{\alpha i}$ are the resolved stresses of each type ($\alpha = E, G$) on each plane ($i = 1, 2$), $\tilde{\sigma}$ is the local stress tensor, and the $\mathbf{S}_{\alpha i}$ are projection matrices.

The stress tensor $\tilde{\sigma}$ is obtained from the linear superposition of the four relevant components considered in Figure 7:

$$\tilde{\sigma} = a\mathbf{S'}_{E1} + b\mathbf{S'}_{G1} + c\mathbf{S'}_{E2} + d\mathbf{S'}_{G2} \tag{9}$$

Here, a, b, c and d are stress factors related to each component and the $\mathbf{S'}_{\alpha i}$ are the Schmidt tensors that give the maximum resolved shear stress of each component on each plane.

However, as defined in eq. 9, the four tensors $\mathbf{S'}_{\alpha i}$ will not necessarily be independent of one another and the application of one isolated component on any one plane may result in a resolved shear stress on the other. This is not in itself an erroneous proposition, as in reality any combination of stresses, independent or not, that produces the desired Peach-Köhler forces is valid. However, for simplicity and mathematical elegance, and other technical reasons that will be discussed below, it is best to find a solution for eq. 8 that renders the $\mathbf{S}_{\alpha i}$ tensors independent through a relation among their projection matrices.

The relation between the $\mathbf{S'}_{\alpha i}$ and the $\mathbf{S}_{\alpha i}$ simply follows from the imposition of orthogonality constraints on the projection matrices in equation 8, *i.e.*:

$$\begin{aligned} \mathbf{S'}_{\alpha i}\mathbf{S}_{\alpha i} &= \mathbf{I} \\ \mathbf{S'}_{\alpha i}\mathbf{S}_{\beta j} &= 0 \end{aligned} \tag{10}$$

In this fashion, we ensure that the $\sigma_{\alpha i}$ are mutually orthogonal and, thus, can be applied independently.

Now, our intention is to explore the four-dimensional (4D) stress space defined by the four components in equation 8 in order to identify the threshold stress hypersurface that marks the transition from glide to cross-slip. Additionally, we are also interested in determining the pertinent cross-slip mechanism, as given in Section II B, under each stress condition. For simplicity, we study the projections of this 4D stress space on the three-dimensional subspaces defined by the combinations of Escaig and glide stress on each plane: *i.e.* σ_{G1}-σ_{E1}-σ_{G2}, σ_{E1}-σ_{G2}-σ_{E2}, σ_{G1}-σ_{G2}-σ_{E2} and σ_{G1}-σ_{E1}-σ_{E2}.

All calculations have been performed for the following geometry: $\mathbf{b} = \frac{1}{2}[1\bar{1}0]$, $\mathbf{n}_1 = (111)$ and $\mathbf{n}_2 = (11\bar{1})$. The length of the initial straight dislocation was of approximately 75 nm. The value ranges for each of the stress components considered was determined from geometric stability conditions such as partial dislocation constriction or runaway partials.

Finally, we have calibrated the cross-slip maps from the minimum glide stress on the secondary plane required to induce cross-slip by a Fleischer mechanism in the absence of any Escaig stress on the primary plane, ($\sigma_{E1} = 0$, $\sigma_{G2} = 2122.6$ MPa). This value is closely related to the energy required to nucleate a stair-rod dislocation in Fleischers' model. Both of these values have been obtained numerically using specifically-designed atomistic simulations and provide physically-based input from which to build the stress maps. In what follows, we make use of this and the parametrization performed in Section III A 1 to construct the

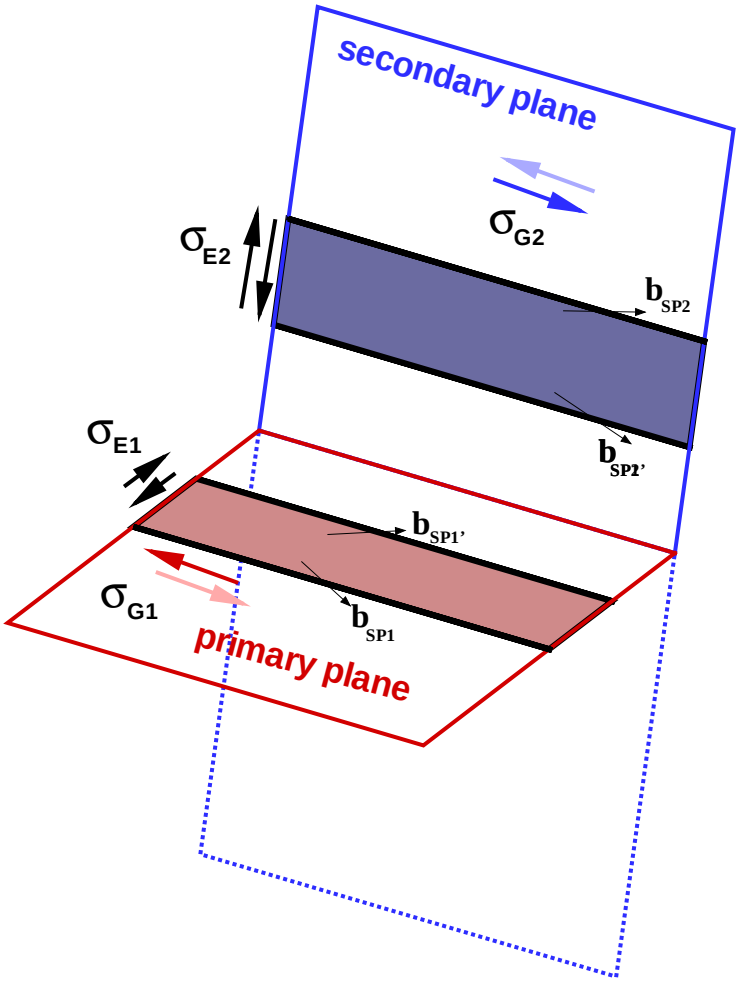

FIG. 7: Schematic diagram showing the geometry of the glide (primary) and cross-slip (secondary) planes with the four relevant components of the stress tensor, namely Escaig and glide stresses on both planes. Shown schematically on each plane are two extended screw dislocations. The shaded stripes are the stacking fault ribbons. Shockley partials are shown in black.

surfaces plotted in Figures 9 to 12. More details about each one of them are given in each corresponding subsection below.

1. Glide and Escaig stress on primary plane; Escaig stress on secondary plane.

The 3D map for this stress combination is plotted in Figure 9. The calculations were performed by relaxing the screw dislocation to the equilibrium distance dictated by the value of σ_{E1} and then applying pairs (σ_{G1},σ_{E2}) to obtain the surface points. The surface obtained

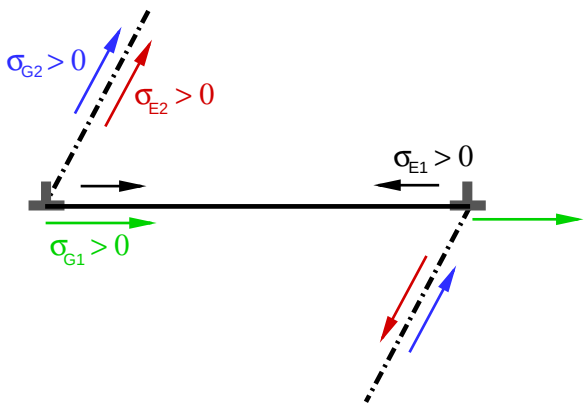

FIG. 8: Schematic view along the dislocation line of the different forces created by the four orthogonal stresses relevant for cross-slip. The direction of the forces shown for each Shockley partial correspond to positive values of the stress. As shown in the figure, in some instances, the stresses produce forces with opposite signs on different partials. This interplay among different stress components governs the cross-slip mechanisms and gives the stress maps shown below.

(in color) represents the locus of the triad σ_{G1}-σ_{E1}-σ_{E2} above which the dislocation is seen to cross-slip by a Fleischer mechanism, *i.e.* no cross-slip occurs below the colored surface. σ_{E1} ranges from the value for runaway partials at -0.0079μ to 0.0316μ at which full constriction is attained in the absence of any other stress components (see Section III A 1).

A salient characteristic of this stress subspace is the absence of cross-slip for negative (separating) Escaig stresses on the secondary plane. The reason is that, with the simulated geometry, only positive values of σ_{E2} will produce acute cross-slip. As we showed in Section III B, obtuse cross-slip is forbidden in our simulations due to, presumably, the high extrinsic stacking fault energy in our Cu model. Therefore, a positive or negative value for σ_{E2} must not be understood strictly in terms of constriction or separation of partials in this case, but, rather, as giving the direction of the force that produces cross-slip in the acute or obtuse sense. Because σ_{E2} acts upon both partials simultanoeusly and in the same fashion, cross-slip with these components always produces anti-symmetric structures such as those shown

in Figure 8. In this sense, the primordial effect of the glide stress on the primary plane is simply to facilitate or hamper (for small and large values of $|\sigma_{G1}|$ respectively) the onset of cross-slip in this subspace. Of course, the cross-slip map is perfectly symmetric with respect to any glide component on either plane, as in the starting configuration the two Shockley partials can be considered indistinguishable for all practical purposes.

The shaded boundary plane at $\sigma_{E1} = 0.0316\mu$ shown in the figure effectively marks the transition from a Fleischer to a Friedel-Escaig cross-slip mechanism for any non-zero value of the stress components acting on the secondary plane. However, because the only component on the secondary plane considered for this subspace is σ_{E2} and, as we showed, this can only take positive values, in order to have Friedel-Escaig cross-slip it is actually required that σ_{E2} be positive. In other words, the mathematical condition that must be satisfied in this stress subspace to have Friedel-Escaig cross-slip is: $(\sigma_{E1} \geqslant 0.0316\mu, \forall\ \sigma_{E2} > 0)$.

The stress surface does not show a strong dependence with σ_{E1}, in particular σ_{G1}, which is virtually independent of σ_{E1}. However, notably, the amount of σ_{E2} needed to induce cross-slip decreases as the dislocation separation distance departs from its equilibrium value at zero Escaig stress on the primary plane.

2. Glide and Escaig stress on primary plane; glide stress on secondary plane.

As pointed out above, all solutions are symmetric with respect to either of the two glide stresses. This is clearly illustrated in Figure 10, where both $\sigma_{G1} = 0$ and $\sigma_{G2} = 0$ are planes of mirror symmetry. In this case, the surfaces shown in the figure represent the loci $\sigma_{G2} = f(\sigma_{G1}, \sigma_{E1})$ above which cross-slip by a Fleischer mechanism occurs. Of course, by virtue of symmetry, the mathematical condition for cross-slip can simply be expressed as $|\sigma_{G2}| \geqslant f(|\sigma_{G1}|, |\sigma_{E1}|)$, *i.e.* cross-slip takes place for stress triads on or above the red surface or on or below the blue surface.

Again in these calculations, any departure from the Shockley partial equilibrium distance towards a more constricted (assisted by $\sigma_{E1} > 0$) or a more extended ($\sigma_{E1} < 0$) state results in an eased cross-slip configuration in terms of σ_{G2}. This is a somewhat puzzling observation, as one would think that the higher energy configurations induced by the Escaig stress might be relaxed by spreading on the cross-slip plane. However, we have checked this observation by simulating equivalent dislocation geometries using molecular dynamics and the atomistic

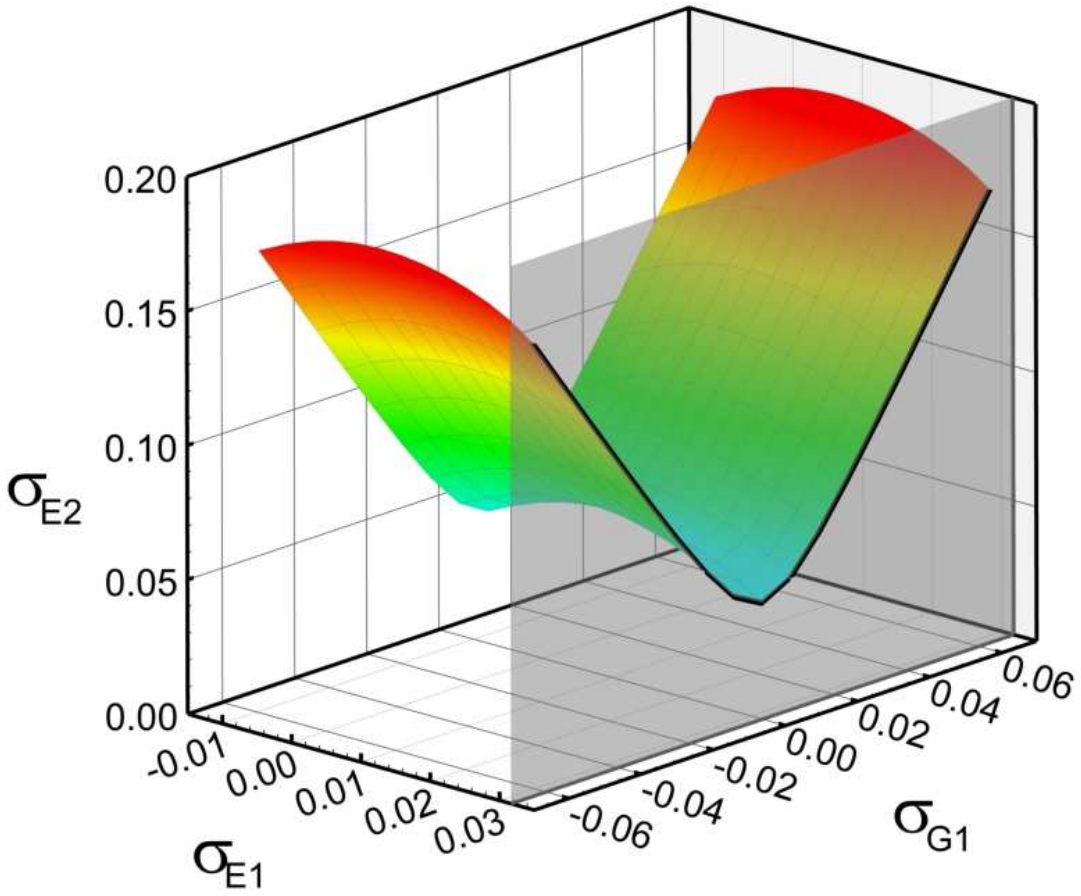

FIG. 9: Three-dimensional stress map for the cross-slip of a perfect screw dislocation from the primary to the secondary plane according to Figure 7 when Escaig stress is applied on both planes and glide stress is only applied on the primary plane. All stresses are normalized to the value of the shear modulus μ. Positive values of σ_{E1} or σ_{E2} indicate constriction stress. Note how σ_{E1} ranges from the value for runaway partials of -0.0079μ to 0.0316μ at which full constriction is attained (shaded plane).

results are consistent with the DD simulations: the stability of the equilibrium configuration appears to provide a slight barrier to cross-slip, which is diminished at once by a deviation in either direction from the equilibrium structure.

As for the previous case, the maximum value of σ_{E1} is that for which full partial dislocation constriction is attained and, hence, the plane $\sigma_{E1} = 0.0316\mu$ marks the transition from Fleischer to Friedel-Escaig for any non-zero value of σ_{G2}.

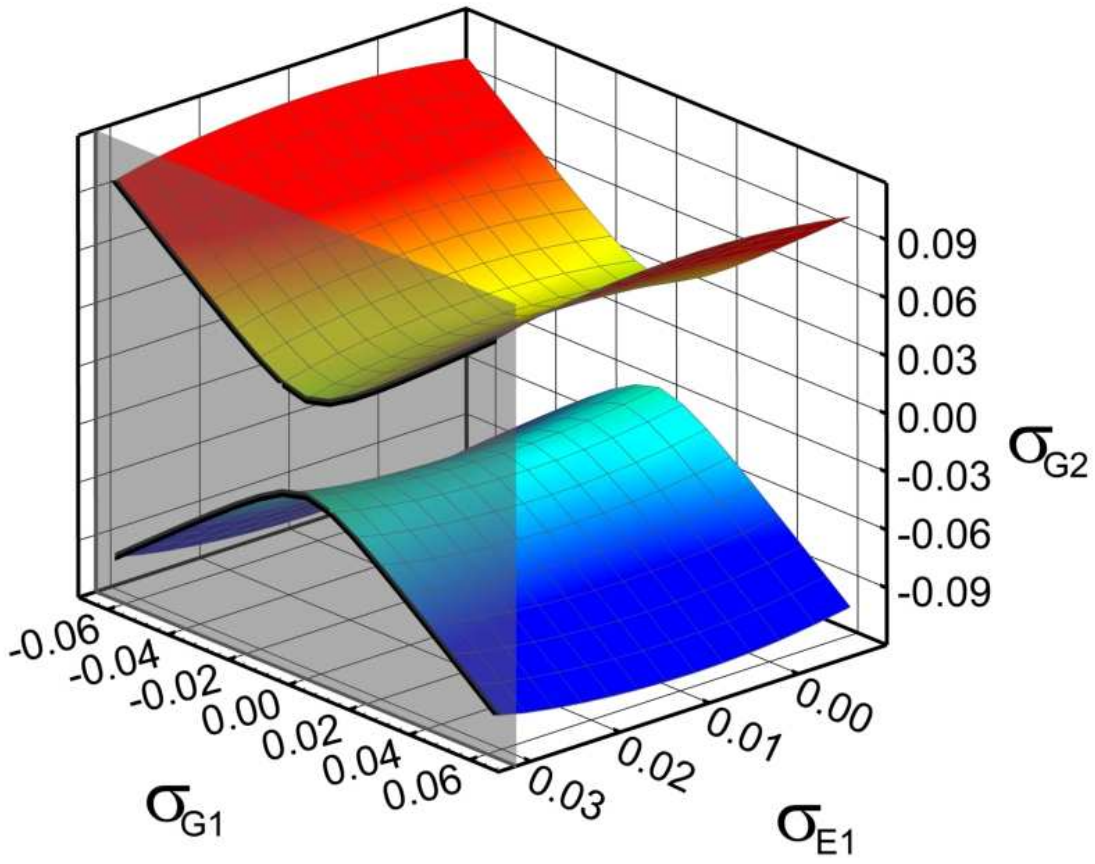

FIG. 10: Three-dimensional stress map for the cross-slip of a perfect screw dislocation from the primary to the secondary plane according to Figure 7 when glide stress is applied on both planes and Escaig stress is only applied on the primary plane. All stresses are normalized to the value of the shear modulus μ. The shaded plane marks the divide between cross-slip by Fleischer and Friedel-Escaig mechanisms.

3. Escaig stress on primary plane; glide and Escaig stress on secondary plane.

The σ_{E1}-σ_{G2}-σ_{E2} map is plotted in Figure 11. In this case, the curves exhibit only one symmetry plane ($\sigma_{G2} = 0$), at which they intersect. This means that for certain combinations of σ_{E1} and σ_{E2} that satisfy the relation $\sigma_{E2} \geqslant f(\sigma_{E1})|_{\sigma_{G2}=0}$, cross-slip by a Fleischer mechanism always occurs regardless of the value of σ_{G2}.

The same effect observed in Section III D 1 regarding Escaig stress on the secondary plane

is also seen here. The sign of σ_{E2} cannot be interpreted in terms of constriction/separation but rather as assisting in inducing acute or obtuse cross-slip. For acute cross-slip (the only one possible) to occur when $\sigma_{E2} < 0$, increasing amounts of glide stress on the secondary plane must be applied to overcome the obtuse cross-slip tendency created by the secondary Escaig stress. Consequently, the cross-slip forces on each partial due to the stress components acting on the secondary plane are additive in one case and opposing in the other, akin to the mechanism shown in Figure 8. Therefore the mathematical condition for cross-slip by a Fleischer mechanism is simply: $(|\sigma_{G2}| + \sigma_{E2} > 0, \forall\ \sigma_{E1})$. Here we also capture the repulsive effect caused by constricted partials on cross-slipped configurations, *i.e.* the higher the value of $|\sigma_{E1}|$, the lower the value of the glide stress on the secondary plane needed to provoke cross-slip.

Here too σ_{E1} ranges between -0.0079μ and 0.0316μ, beyond which, respectively, we have runaway partials and Friedel-Escaig cross-slip. The mathematical condition required for Friedel-Escaig cross-slip in this case is: $(\sigma_{E1} \geqslant 0.0316\mu, \forall\ \sigma_{E2}, \sigma_{G2} > 0)$.

4. Glide stress on primary plane; glide and Escaig stress on secondary plane.

The stress surface corresponding to the σ_{G1}-σ_{G2}-σ_{E2} map is shown in Figure 12. Here again two planes of symmetry exist, as corresponds to having both glide components active. With this stress combination, no cross-slip by a Friedel-Escaig mechanism can ever occur, as, in the absence of any σ_{E1}, the orthogonality conditions 10 prevent any constricting stresses to develop on the primary plane.

In this case, the effect of having Escaig stress on the secondary plane is also to direct cross-slip in the acute ($\sigma_{E2} > 0$) or obtuse ($\sigma_{E2} < 0$) senses. Since obtuse cross-slip is forbidden, a negative σ_{E2} must be overcome by the secondary glide stress acting in the opposite direction so that acute cross-slip can occur. That is why the surfaces exhibit an increasing trend for negative values of the secondary Escaig stress. At $(\sigma_{G1}, \sigma_{E2} = 0)$, σ_{G2} takes the calibrated value of 2122.6 MPa (0.034μ). With respect to the σ_{G1}-σ_{E2} dependency, similar to the case in Section III D 1, there is only a very weak coupling between these two stress components.

Lastly, the $\sigma_{G2} = f(\sigma_{G1})$ relation is of hyperbolic type, such that for increasingly larger values of $|\sigma_{G1}|$, $|\sigma_{G2}|$ must be increased to overcome the inertial resistance of the dislocation

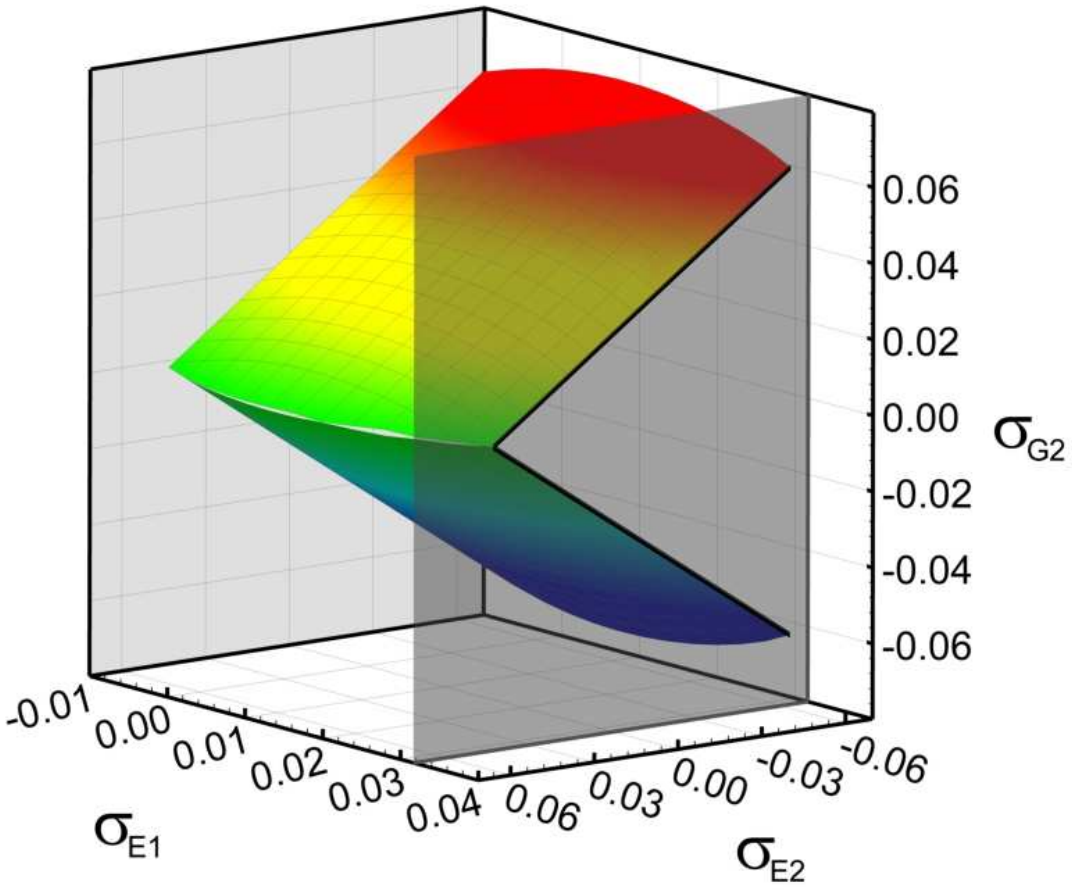

FIG. 11: Three-dimensional stress map for the cross-slip of a perfect screw dislocation from the primary to the secondary plane according to Figure 7 when Escaig stress is applied on both planes and glide stress is only applied on the cross-slip plane. All stresses are normalized to the value of the shear modulus μ. The shaded plane indicates the divide between cross-slip by Fleischer and Friedel-Escaig mechanisms.

to cross-slip. As for the previous cases where σ_{E2} is present, the cross-slip mechanism in this case is a combination of glide and Escaig on each partial, synergistic for one of them and competing for the other (Figure 8).

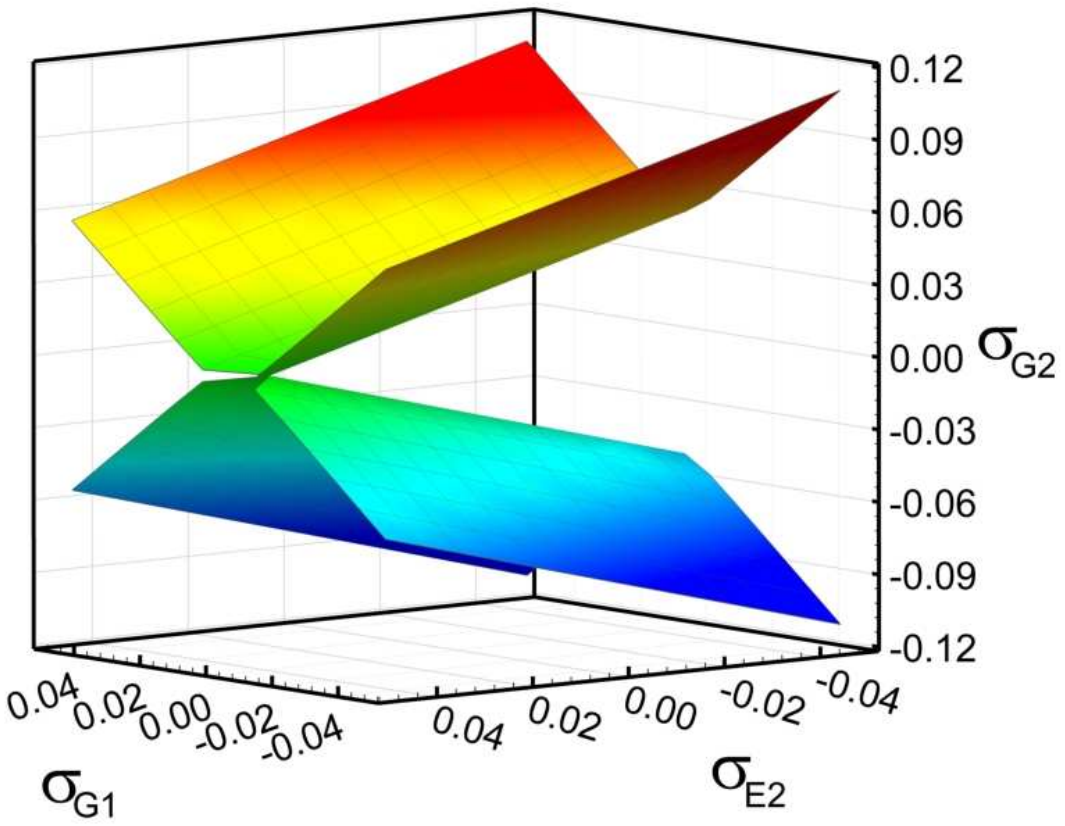

FIG. 12: Three-dimensional stress map for the cross-slip of a perfect screw dislocation from the primary to the secondary plane according to Figure 7 when glide stress is applied on both planes and Escaig stress is only applied on the cross-slip plane. All stresses are normalized to the value of the shear modulus μ.

IV. DISCUSSION

Brief discussions of the methods and the results for each section have been provided in Section III. Below we elaborate on the implications extracted form this work in terms of the fitting procedure, the dislocation junctions considered and cross-slip.

A. Fitting procedure and Shockley partial separation distance

The only material parameters present in our method are the shear modulus, μ, the stacking fault energy, γ, and the dislocation core width, a, extracted from the non-singular elastic formulation described in Section I A. To obtain appropriate values for μ, γ and a, commensurate with the type of calculations that we have carried out, we have devised a fitting procedure based upon atomistic simulations designed around a state-of-the-art interatomic potential for Cu. Ostensibly, the main objective of the fitting procedure is not to produce accurate values for the materials parameters (although this may very well occur as an indirect consequence of the fitting), but to provide a meaningful physical framework within which to parameterize our methodology. Here, the shear modulus and stacking fault energy are simply taken from experimental values (via the interatomic potential), and have not required any further treatment except the rotation of μ to the specific geometry of fcc slip. The core width, on the other hand, is amenable to several types of fitting schemes, all requiring atomistic approaches of one kind or another to deal with core non-linearities. For example, a very common practice is to take a as twice the distance over which $\pm\frac{b}{4}$ is seen to spread, although the criterion to estimate the core width is generally quite arbitrary and there is no established way to do it. In any case, here we have chosen a two-fold fitting process:

- First, a is chosen so as to ensure consistency between DD and MD calculations of Shockley partial equilibrium separation (Figure 3).

- Secondly, once the value of a was established to $1.75b$, we calculated the corresponding core energies for all possible dislocation partials

In this fashion, by rotating μ to our particular geometry, we are able to introduce a certain degree of 'anisotropy' in our simulations. Similarly, by including core energetics in our simulations we have taken the step towards fully incorporating core effects in dislocation dynamics. At present, core energies are simply used to fit an analytical expression that gives a non-glide self-force on each segment[25]. In calculating the specific values for each type of dislocation, we now have a more accurate representation of the forces governing the line stiffness.

A direct validation of our fit is provided by the equlibrium separation distance at zero Escaig stress in Figure 3, with the DD curves almost exactly matching the MD result of 2.0087 nm. Another useful validity check is shown in Figure 4. In it we plot the Shockley partial separation curves for pure edge, 60° and 30° mixed dislocations as obtained with the fitted values for the perfect screw. The zero-stress crossings can be compared to the MD results by Henager and Hoagland[35] with satisfactory agreement.

B. Dislocation junctions

Current models for the strain hardening of crystals in multislip conditions are based on the properties of junctions, which has resulted in considerable efforts to study the dislocation reactions leading to junction formation and characterize their relative strengths. In fcc crystals, the well-known scaling law between the stress and the square root of the dislocation density is found to hold experimentally over a fairly large stress range, even in conditions where the dislocation density is heterogeneous and patterns are formed[7]. This law hinges on a set of hardening coefficients (see equation 6) that can be either be calculated directly by a number of methods or can be inferred from plasticity experiments and large-scale dislocation dynamics simulations. In this sense, our calculations in Section III B suggest that, for the conditions chosen in our study, the co-linear junction is the strongest, followed by the co-planar, Lomer-Cottrell and Hirth locks. Nevertheless, the strength of a particular type of lock does not necessarily correlate with its relative importance in terms of plastic hardening, as other factors such as loading condition, occurrence, reacting geometry, etc., have a strong effect on the plastic relevance of each junction. The appropriate method to estimate the true importance of each junction is to separate their relative contribution to the total hardening (as measured via equation 6) in large-scale DD plasticity simulations. This has been the approach employed by a number of workers, most notably Madec *et al.*[44] and Devincre *et al.*[18], who have come up with self-consistent ways to differentiate among each fcc lock in their simulations. Their conclusions, interestingly, confirm the first-order assumption (which also emanates from our results) that there might be a direct correspondance between junction strength and their comparative contribution to hardening.

Of course, each junction is only fully characterized by way of its yield curve, which gives the junction strength in some stress space, usually pure glide in the glide and forest planes.

Here we have only computed three points of the yield curve, the most representative in our view, and thus our findings are framed within this simplified representation of the fcc locks. Yield curves using elastic models have been published[13,17], with reasonable qualitative agreement with our results. Dupuy and Fivel[13] have computed the yield curves for the Lomer-Cottrell, glissile and Hirth locks and find that the glissile (co-planar) junction is weaker than the Lomer-Cottrell for a number of geometries explored. Interestingly, they give a closed co-planar yield curve, something inconsistent with our definition for this junction (see Figure 5), which presumes that it is always stable with respect to any stresses on the forest plane and can only be dissolved when the stress applioed on the glide plane overcomes the glissile tendency of the junction on the forest plane.

Another important aspect to consider is the fact that the rate of work hardening in stage II deformation, θ_{II}, appears to be approximately universal and equal to $\sim \frac{\mu}{300}$. Despite the large uncertainties present in these empirical relations, these models are formulated independently of the stacking fault energy of the material or the zipping length over which the junction occurs. In other words, what this suggests, indirectly, is that all ths is needed to study stage II hardening are purely elastic models that neglect core effects and/or dislocation dissociation into partials. Quite to the contrary, recent DD simulations[49], seem to provide evidence that the core's contribution to the nodal self-energy has an important effect on the strength of junctions. The only way to shed more light on this is by performing studies of junction formation and dissolution with methods that resolve the dislocation core explicitely, *e.g* methods capable of atomistic resolution. Indeed, there have been numerous works focusing on one specific type of junction tha explicitely account for core energetics and structure[12,42,43,50], the disadvantage being that these studies are numerically quite expensive. Hence, our method suggests itself as an intermediate solution between fully-resolved but costly atomistic calculations and more coarsened approaches that usually disregard core energetics.

C. Cross-slip

In fcc materials, the traditional view is that cross-slip is enabled when the stress buildup arising from forest and precipitation hardening is high enough for screw dislocations to escape their obstacles by gliding on a plane different than their original slip plane (the so-called

stage III). Because dislocations are dissociated on {111} planes in fcc systems, cross-slip has relatively high activation energies and volumes, and efforts to calculate them have generally not been very successful until recently with the advent of atomistic methods.

Jackson[51] and, more recently, Püschl[32] (and references therein) have published comprehensive reviews covering the theoretical and experimental aspects of cross-slip in fcc metals. Invariably in these works, the inherent limitations of linear elasticity at distances close to the dislocation core are identified as the cause why continuum analytical models have failed to provide an accurate description of cross-slip, both in terms of the computed activation parameters, and also in the range of geometries explored. In response to this shortcomings, and with the advent of reliable interatomic potentials, atomistic methods have been recently used to study cross-slip in some aspect or another. The most notable works have been by Duesbery[52], Rao *et al.*[53] and Rasmussen *et al.*[54,55]. The advantage of using atomistics is that these methods provide very detailed insights into the transition paths conducive to cross-slip without too many *a priori* assumptions. However, difficulties still remain, mostly associated to the treatment of far-reaching dislocation stress fields and the quality of the potentials employed. Whichever the case, however, we are not aware of any published work in the available literature that provides a comprehensive picture of cross slip as a function of the relevant stress components.

In this sense, because our methodology makes use of a non-singular elastic formulation fitted to atomistic data, it does not suffer from the short-range elastic divergence found in other linear elastic models. This, combined with the dislocation dissociation scheme developed here, has allowed us to study in detail the dynamics of cross-slip and discern among the different mechanisms being considered in the literature. Aided by the computational expediency of DD —when compared to atomistic methods—, we have been able to obtain the detailed stress maps shown in Figs. 10 to 12, which, for the first time, provide a simple and effective criterion for cross-slip solely in terms of the *remote* stress state. However, in addition to their inherent numerical value, two important physics findings emanate from these stress maps. Firstly, we have discovered that the application of Escaig stress is an impediment, albeit small, to cross-slip by a Fleischer mechanism, irrespective of the sign of σ_{E1}. In other words, there exist minima at $\sigma_{E1} = 0$ in the relations of the primary Escaig stress with the secondary stress components σ_{G2} and σ_{E2}. We argue that this is due to the relative stability of stress-free dislocations vs. their constricted or extended configurations.

More calculations are needed, however, to prove or disprove this extent. Secondly, our results may narrow down the number of possible pathways for dislocation annihilation in Kubin *et al.*'s recent study on plastic recovery[56] by removing the plausability for obtuse cross-slip. As shown in Sections III B and II B, we have demonstrated both using MD and DD simulations that, at least for Cu, the energy cost of creating extrinsic faults precludes the formation of inverse junctions (*e.g.* obtuse Lomer-Cottrell or acute Hirth locks) and obtuse cross-slip.

However, it is still difficult at this point to identify a direct means to validate our simulations, other than perhaps using atomistic results where available. Ultimately, these stress maps will have to be incorporated into large-scale DD crystal plasticity simulations and the results benchmarked against existing experimental databases.

The remaining, and final, issue concerning cross-slip in fcc metals is to produce a full energy landscape of the cross-slip process as a function of stress so that thermal effects can be incorporated into the simulations. This can in principle be achieved by way of atomistic calculations (the atomistic works referenced in the previous paragraphs are essentially zero-stress calculations of these energies), although the associated computational cost can be daunting, or, now that we possess information about core energies (Table I), using fast DD simulations to calculate configuration energies as a function of dislocation position and character.

V. CONCLUSIONS

In summary, we have extended the discrete dislocation dynamics methodology as developed by Bulatov and co-workers[25] to fcc systems by explicitely considering all dislocation dissociations and reactions among partials. To this end, we have derived simple continuity laws that enable the treatment of stacking faults and partial dislocation nodes. In addition, we have added appropriate topological rules to account for the specific transformations relevant to fcc slip, *e.g.*, dislocation dissociation, junction formation, cross-slip, etc. Our dislocation dynamics methodology has been fitted to atomistic results in Cu, including core energetics, and has withstood the test of several simple validation checks. We show that, consistent with real crystals, the parameter governing dislocation dissociation is the stacking fault energy.

We have obtained the dissolution strengths of the main four dislocation junctions in fcc

metals, namely the Lomer-Cottrell, Hirth, co-linear and co-planar junctions, and find that, in agreement with the current state-of-the-art in DD simulations, the co-linear junction is clearly the strongest.

We have characterized the four-dimensional cross-slip surface by mapping threefold stress subspaces and have extracted simple mathematical rules to implement the different cross-slip mechanisms considered. Based on atomistic simulations, our model does not include cross-slip into obtuse planes, as the stress required for this process is significantly larger than for the acute case. The thermally-activated nature of cross-slip has not been treated here and our stress surfaces provide a cross-slip map in zero-temperature equivalent conditions. Future work includes computing the cross-slip energy landscape as a function of the applied stress so that thermal effects can be accounted for.

Acknowledgments

Work performed under the auspices of the U.S. Department of Energy by the University of California Lawrence Livermore National Laboratory under contract No. W-7405-ENG-48 and the Laboratory-directed Research and Development Office under program 06-ERD-005.

---

[1] B. Devincre and L. Kubin, Mater. Sci. Eng. A **8**, 234 (1997).

[2] K. W. Schwarz, J. Appl. Phys. **85**, 108 (1999).

[3] N. M. Ghoniem and L. Z. Sun, Phys. Rev. B **60**, 128 (1999).

[4] V. V. Bulatov, M. J. Tang, and H. M. Zbib, MRS Bulletin **26**, 191 (2001).

[5] H. M. Zbib, T. D. de la Rubia, M. Rhee, and J. P. Hirth, J. Nucl. Mater. **276**, 154 (2000).

[6] W. Cai, V. Bulatov, T. Pierce, M. Hiratani, M. Rhee, M. Bartelt, and M. Tang, *Massively-parallel dislocation dynamics simulations*, vol. 115 (Kluwer Academic Publisher, Dordrecht, 2004).

[7] L. P. Kubin, B. Devincre, and M. Tang, J. Comp.-Aided Mat. Des. **5**, 31 (1998).

[8] H. M. Zbib and T. D. de la Rubia, Int. J. Plast. **18**, 1133 (2002).

[9] N. G. Pharr and W. D. Nix, Acta Metall. **27**, 433 (1979).

[10] L. P. Kubin, R. Madec, and B. Devincre, in *Mater. Res. Soc. Symposium Proceedings* (Warrendale, PA, USA, 2003), vol. 779, p. 25.

[11] M. Verdier, M. Fivel, and I. Groma, Modelling Simul. Mater. Sci. Eng. **6**, 755 (1998).

[12] V. B. Shenoy, R. V. Kukta, and R. Phillips, Phys. Rev. Lett. **84**, 1491 (2000).

[13] L. Dupuy and M. C. Fivel, Acta Mater. **50**, 4873 (2002).

[14] R. Madec, B. Devincre, and L. P. Kubin, Phys. Rev. Lett. **89**, 255508 (2002).

[15] C. Depres, M. Fivel, C. Robertson, A. Fissolo, and M. Verdier, J. Physique IV **106**, 81 (2003).

[16] M. A. Shehadeh, H. M. Zbib, and T. D. de la Rubia, Philos. Mag. **85**, 1667 (2005).

[17] C. S. Shin, M. C. Shivel, D. Rodney, R. Phillips, V. B. Shenoy, and L. Dupuy, J. Phys. IV France **11**, 5 (2001).

[18] B. Devincre, L. Kubin, and T. Hoc, Scripta Mater. **54**, 741 (2006).

[19] K. Hardikar, V. Shenoy, and R. Phillips, J. Mech. Phys. Solids **49**, 1951 (2001).

[20] V. Vitek, Trans. Indian. Inst. Met. **38**, 510 (1985).

[21] J. F. Justo, V. V. Bulatov, and S. Yip, Scripta Mater. **36**, 707 (1997).

[22] R. LeSar, Phys. Status Solidi (b) **241**, 2875 (2004).

[23] J. Lothe and J. P. Hirth, Phys. Status Solidi (b) **242**, 836 (2005).

[24] W. Cai, A. Arsenlis, C. R. Weinberger, and V. V. Bulatov, J. Mech. Phys. Solids **54**, 561 (2006).

[25] V. V. Bulatov, W. Cai, J. Fier, M. Hiratani, T. Pierce, M. Tang, M. Rhee, K. Yates, and A. Arsenlis, *Scalable line dynamics of ParaDiS, SuperComputing 19* (2004), http://www.sc-conference.org/sc2004/schedule/pdfs/pap206.pdf.

[26] M. de Koning, W. Cai, and V. V. Bulatov, Phys. Rev. Lett. **91**, 025503 (2003).

[27] G. Shoeck and A. Seeger, *Defects in Crystalline Solids* (Physical Society, London, 1955).

[28] J. Friedel, *Dislocations and Mechanical Properties of Crystals* (Wiley, New York, 1957).

[29] B. Escaig, J. Physique **29**, 225 (1968).

[30] R. L. Fleischer, Acta Metall. **7**, 134 (1959).

[31] M. J. Cawkwell, D. Nguyen-Manh, C. Woodward, D. G. Pettifor, and V. Vitek, Science **309**, 1059 (2005).

[32] W. Puschl, Prog. Mat. Science **47**, 415 (2002).

[33] D. Caillard and J. L. Martin, J. Phys. France **50**, 2455 (1989).

[34] W. Cai, V. V. Bulatov, J. Chang, J. Li, and S. Yip, Phys. Rev. Lett. **86**, 5727 (2001).

[35] C. H. Henager and R. G. Hoagland, Philos. Mag. **85**, 4477 (2005).

[36] Y. Mishin, M. J. Mehl, D. A. Papaconstantopoulos, A. F. Voter, and J. D. Kress, Phys. Rev. B **63**, 224106 (2001).

[37] J. Marian and A. Caro, Phys. Rev. B **74**, 024113 (2006).

[38] J. Li, C.-Z. Wang, J.-P. Chang, W. Cai, V. V. Bulatov, K.-M. Ho, and S. Yip, Phys. Rev. B **70**, 104113 (2004).

[39] V. V. Bulatov, S. Yip, and A. S. Argon, Phil. Mag. A **72**, 453 (1995).

[40] P. Franciosi, M. Berveiller, and A. Zaoui, Acta Metall. **28**, 273 (1980).

[41] J. P. Hirth, J. Appl. Phys. **32**, 700 (1961).

[42] S. J. Zhou, D. L. Preston, P. S. Lomdahl, and D. M. Beazley, Science **279**, 1525 (1998).

[43] D. Rodney and R. Phillips, Phys. Rev. Lett. **82**, 1704 (1999).

[44] R. Madec, B. Devincre, L. Kubin, T. Hoc, and D. Rodney, Science **301**, 1879 (2003).

[45] J. P. Hirth and J. Lothe, *Theory of Dislocations* (Krieger Publishing Company, Malabar, Florida, 1992).

[46] Y. Q. Sun, P. M. Hazzledine, M. A. Crimp, and A. Couret, Philos. Mag. A **34**, 311 (1991).

[47] J. Bonneville and G. Vanderschaeve, Philos. Mag. Lett. **78**, 87 (1998).

[48] D. Hull and D. J. Bacon, *Introduction to Dislocations, 3*$^{\rm rd}$ *Edition* (Butterworth-Heinemann, Oxford, UK, 1984).

[49] A. Arsenlis, W. Cai, M. Tang, M. Rhee, T. Oppelstrup, M. Hiratani, G. Hommes, T. G. Pierce, and V. V. Bulatov (2006).

[50] V. V. Bulatov, B. D. F. F. Abraham, L. Kubin, and S. Yip, Nature **391**, 669 (1998).

[51] P. J. Jackson, Prog. Mat. Science **29**, 139 (1984).

[52] M. S. Duesbery, Modelling Simul. Mater. Sci. Eng. **6**, 35 (1998).

[53] S. Rao, T. A. Parthasarathy, and C. Woodward, Philos. Mag. A **79**, 1167 (1999).

[54] T. Rasmussen, K. W. Jacobsen, T. Leffers, O. B. Pedersen, S. G. Srinivasan, and H. Jonsson, Phys. Rev. Lett. **79**, 3676 (1997).

[55] T. Rasmussen, K. W. Jacobsen, T. Leffers, and O. B. Pedersen, Phys. Rev. B **56**, 2997 (1997).

[56] L. P. Kubin, B. Devincre, and T. Hoc, Philos. Mag. **86**, 4023 (2006).

[57] Generally, dislocation theory books depict SFT formation as a process in which Shockley partial reaction on the edges lags glide on the {111} planes, reason why segments on the planes appear as bulging out.

TABLE II: Geometry and strength of the Lomer-Cottrell, Hirth and co-planar junctions. The relative geometries are given in terms of the Thompson tetrahedron. The values for the strength correspond to the σ_1 points of the yield curve for which no stress is applied on the forest plane ($\sigma_2 = 0$). point in the yield curve for the Lomer-Cottrell, Hirth and co-linear junctions, and the $(\sigma_1, 0)$ point for the co-planar junction (see text). The **b** and γ**n** reactions are also shown for reference.

Junction type	Reactions	Strength (μ)
Lomer-Cottrell		
(geometry)	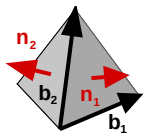	0.0071
(**b** reaction)	$\frac{1}{2}[\bar{1}10] + \frac{1}{2}[101] \rightarrow \frac{1}{2}[011]$	
(γ**n** acute reaction)	$\frac{1}{\sqrt{3}}[\bar{1}\bar{1}\bar{1}] + \frac{1}{\sqrt{3}}[1\bar{1}\bar{1}] \rightarrow \frac{1}{\sqrt{3}}[0\bar{2}\bar{2}]$	
Hirth		
(geometry)	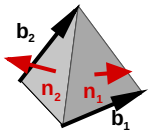	0.0042
(**b** reaction)	$\frac{1}{2}[\bar{1}10] + \frac{1}{2}[\bar{1}\bar{1}0] \rightarrow \frac{1}{6}[\bar{2}1\bar{1}] + \frac{1}{6}[\bar{2}\bar{1}1] + \frac{1}{3}[\bar{1}00]$	
(γ**n** obtuse reaction)	$\frac{1}{\sqrt{3}}[\bar{1}\bar{1}1] + \frac{1}{\sqrt{3}}[1\bar{1}\bar{1}] \rightarrow \frac{1}{\sqrt{3}}[0\bar{2}0]$	
Co-planar		
(geometry)	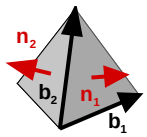	0.0104
(**b** reaction)	$\frac{1}{2}[1\bar{1}0] + \frac{1}{2}[\bar{1}0\bar{1}] \rightarrow \frac{1}{6}[112] + \frac{1}{6}[\bar{1}21]$	
(γ**n** acute reaction)	$\frac{1}{\sqrt{3}}[\bar{1}\bar{1}\bar{1}] + \frac{1}{\sqrt{3}}[\bar{1}\bar{1}1] \rightarrow \frac{1}{\sqrt{3}}[\bar{2}\bar{2}0]$	
Co-linear		
(geometry)	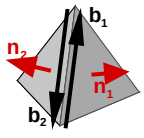	0.0155
(**b** reaction)	$\frac{1}{2}[1\bar{1}0] + \frac{1}{2}[\bar{1}10] \rightarrow$ local annihilation	
(γ**n** acute reaction)	$\frac{1}{\sqrt{3}}[\bar{1}\bar{1}\bar{1}] + \frac{1}{\sqrt{3}}[\bar{1}\bar{1}1] \rightarrow \frac{1}{\sqrt{3}}[\bar{2}\bar{2}0]$	